Ali Mahdi, BSc

ELECTRON BEAM FREEFORM FABRICATION OF Ni-RICH NiTi SHAPE MEMORY ALLOYS: INFLUENCE OF PROCESSING PARAMETERS ON THE STRUCTURE AND FUNCTIONAL PROPERTIES

MASTER'S THESIS

to achieve the university degree of

Diplom-Ingenieur

Master's degree programme:

Production Science and Management

Submitted to

Graz University of Technology

Supervisor

Univ.-Prof. Dr.-Ing. Sergio de Traglia Amancio Filho

Institute of Materials Science, Joining and Forming - IMAT

Aviation Group

Co-supervisor

Eng. Mestre Rafael Paiotti M. Guimaraes

Graz, November of 2020

AFFIDAVIT

I declare that I have authored this thesis independently, that I have not used other than the declared sources/resources, and that I have explicitly indicated all material which has been quoted either literally or by content from the sources used. The text document uploaded to TUGRAZonline is identical to the present master thesis.

Date, Signature

Abstract

Wire-based additive manufacturing technique has arisen as a viable alternative to produce mid-size near-net shape part when compared to powder-based ones. The use of electron beam as an energy source made wire-based processes even more attractive, since the manufacturing takes place in a vacuum chamber and thus the material is protected from deleterious impurity pick-up. Furthermore, the processing of reflective materials, such as titanium and aluminum - important structural materials -, is energetically more favorable once the high intensity electron beam is not reflected by them. Therefore, wire-based electron beam additive manufacturing (or electron beam freeform fabrication – EBF3) gained momentum in the last decades.

The employ of NiTi shape memory alloys - due to its functional and unique properties, namely strain recovery - has been broaden with the support of additive manufacturing. Nonetheless, the processing of NiTi by wire-based techniques is barely explored, thus opening a new branch for investigations. This thesis aims to evaluate the effects of processing parameters on the structural integrity on one, five and ten layer one track stacks of NiTi produced by EBF3. For this purpose, statistical analysis based on the Box-Behnken design of experiments was employed taking into consideration beam current, and welding and feeding speeds as responses. The characterization is based on calorimetry and microscopic analysis. For the selection of the most suitable processing parameter energetic aspects, metallurgical features, and stability of the deposited stacks were taking into consideration. The right manufacturing parameters made possible to build five tracks wide and ten layers high multitrack structure, resulting in total of 50 beads.

TABLE OF CONTENTS

LIST OF FIGURES

LIST OF TABLES

LIST OF SYMBOLS AND ABBREVIATIONS

Symbol	Meaning
E	Specific energy
Ub	Feeding speed
Ws	Welding speed
A	Wire cross section area
Ev	Energy density
X	Deposition rate
ƛ	The ratio of feeding speed to welding speed
DSC	Differential Scanning Calorimetry
X-ray	X-ray diffraction
DoE	Design of Experiments
BBD	Box-Behnken design of Experiments

Introduction

Additive manufacturing (AM), also known as rapid manufacturing or rapid prototyping, is a technique based on the printing of parts from a computer-aided design (CAD) or 3D model, aiming to build customized and complex geometrical parts not attainable by conventional extractive manufacturing. As attractive features, AM presents itself cost-effective, has a short lead time, wastes less material if compared to subtractive fabrication methods, and since no pollutants are emitted during fabrication is also an environment-friendly process.

Many studies in the recent years have focused on this method due to its economic importance and commercial interest in fabricating expensive and complex parts [1–4]. There are no cutting tools, fixtures, or machining steps are reduced or absent in comparison to conventional processes, such as casting and forging. Therefore, additive manufacturing came as an alternative technique used to process materials with complex behavior, such as NiTi (Nickel-Titanium) shape memory alloys (SMA) [5].

NiTi and NiTi-based alloys (for instance NiTiHf) have been widely employed in aerospace and biomedical fields in reason of its biocompatibility, corrosion resistance, high stiffness, and two unique functional properties: shape memory effect (SME) and superelasticity (SE). Both are based on the strain recovery after deformation, being activated by heat (shape memory effect) or stress release (superelasticity) [6] However, despite giving NiTi unique importance due to these functional properties, both became NiTi processing by conventional subtractive methods (e.g. machining) a big challenge due to the resistance to deformation, shape recovery and sprig back effect [7]. In addition, the high reactivity of NiTi alloys to high temperature also makes its thermomechanical work complex and difficult, affecting directly the quality and final price of the product [8] .

AM have shown the potential to minimize the aforementioned drawbacks fabricating complex parts and keeping the functional properties. Among the available techniques, either powder or wire based, laser powder bed fusion, popularly known as selective laser melting, has been widely explored and is by far the most successful AM technique for manufacturing small and complex NiTi parts [7,9,12]. Nonetheless, the usage of powder has disadvantages such as high impurity (C, O and N) pickup, which can significantly affect the martensitic transformation temperature and thus change

the mechanical behavior of the part, feedstock losses [13] - configuring extra costs given the high prices of NiTi alloys - and size limitation.

If larger parts are aimed, directed energy deposition processes, such as wire-based AM, has proved its feasibility. By employing wire as a feedstock, the losses decrease practically to zero. In addition, if electron beam is used as an energy source, the impurity pickup is mitigated due to the processing in vacuum [14]. Moderate part geometry complexity is achieved by using wire-based AM, and secondary activities are often necessary to achieve the final shape. Even though, wire-based electron beam additive manufacturing – or electron beam freeform fabrication (EBF3) – succeeded as a manufacturing technique for nickel, titanium and aluminum based alloys [15–19] and gained momentum in the industry [20].

EBF3 has been developed by NASA since the beginning of the 2000's and achieved maturity as an AM process. The main idea behind its development was the production in loco of sparing parts during space missions, enabling the spacecraft to carry less weight and hence save fuel. For this purpose, wire was considered as a feedstock due to its easy handling and reduced wasting, and electron beam as an energy source since vacuum is required for proper operation. Since then, several studies were performed on this technology on, e.g., its physical aspects [21], processing maps [22], and manufacturing of dissimilar parts, such as Cu/steel [23]. The manufacture of NiTi by (EBF3) is a young topic [24], thus a new niche on AM was recently opened.

Aiming to explore the feasibility of NiTi AM by this technique, the present study processed a superelastic Ni-rich NiTi alloy. Statistical analysis based on Box-Behnken Design (BBD) and Analysis of Variance (ANOVA) was performed, and 17 single-track depositions of one, five and ten layers were carried out. Based on the results, it was possible to explain the effects of the main process parameters beam current, feeding speed and welding speed in four responses: layer height and width, dilution, and martensitic starting temperature. In addition, the interaction between each process parameter resulted a reduced equation for each of the four aforementioned responses – or a reduced statistical model –, validated with additional depositions thereby showing its reliability. As a main objective, the optimization of deposition parameters was based on a strict evaluation taking into consideration the energy density of the heat source, low dilution, reduced Ni evaporation, and geometrical aspects of the deposited stacks. The optimized processing parameter were employed on the

manufacturing of multi-track structures, showing its effectiveness and hence the possibility of producing larger parts for mechanical assessment in the future.

1. Theoretical Background

1.1 NiTi shape memory alloys

Shape memory or smart alloy was discovered by Arne Ölander back in 1932. In 1941, Vernon presented the term ‘shape memory’ for his polymeric dental material. William Boehler and Frederik Wang has disclosed the shape memory effect in Ni-Ti alloy (or Nitinol) in 1962, leading to an increase in the demands for SMA especially in industrial and technical fields [25]. Many types of SMA are commercially available, such as NiTi, CuZn, and FeMn based alloys, being NiTi the first SMA commercially invested and intensively studied [6]. The main applications of NiTi are found in the biomedical industry, where cardiovascular stents are widely employed, and in the aerospace fields, in which morphing wings and smart structured have gained visibility in the last decades.

If compared to the other SMA, NiTi alloy attracted much attention due to its superior shape memory and superelastic effects. It means that the shape recovery achieved by both functional effects after deformation is larger: for the superelastic effect 10% [5] if compared to Cu-based alloys with 6% [26]. Besides, NiTi alloys present excellent corrosion resistance, high biocompatibility, excellent ductility, and good fatigue properties [6]. On the other hand, despite excellent functional, physical and mechanical properties, NiTi is extremely expensive if compared to Fe and Cu based alloys and has a complex fabrication route; this fact limits its applications. It boosted the search of new manufacturing routes, such as AM.

1.1.1 Shape memory and superelastic effects

The thermal (shape memory) and the mechanical (superelastic) effects are based on reversible solid-state phase transformation, presenting different deformation modes of martensite (shape memory effect) or austenite (superelasticity) [27]. It causes reorientation of the lattice, thus enabling the memory effects as depicted in Figure 1.

SME is defined as the ability of a material to recover its previous shape when heated after being deformed, prompting the occurrence of phase transformation from martensite to austenite and transforming thermal energy into mechanical work. This phenomenon is illustrated in Figure 1(a), where by mechanically deforming the low-

temperature martensite and subsequently heating it up beyond A_f, the lattice is rearranged and the original shape is recovered. In the case of SE, the alloy can be bent or stretched to great extent in the austenitic state, returning to its original shape once the load is released, as depicted in Figure 1(b). Above A_f and below M_d this load leads to stress induced martensitic transformation, which is reverted upon unloading returning the material to its original shape [7,43,45].

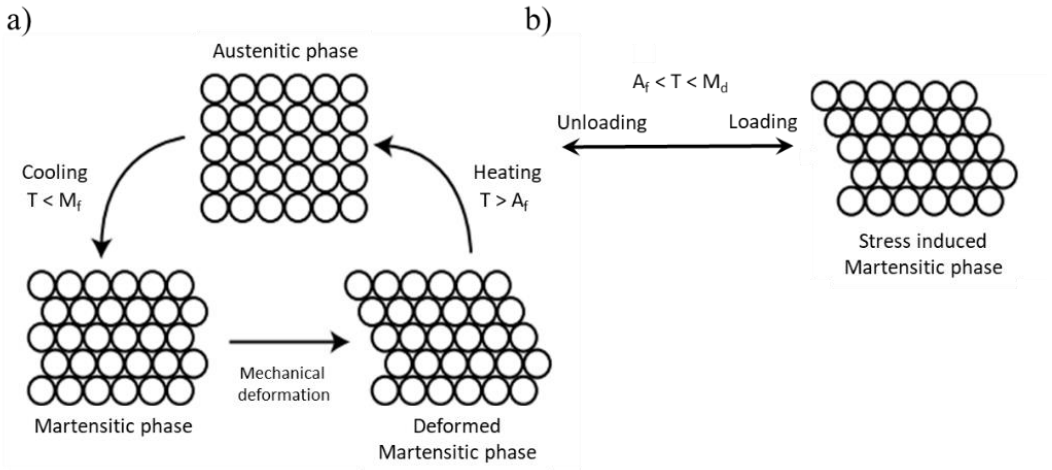

Figure 1. a) Shape memory effect and b) superelasticity in SMA (adapted from ([6])).

SME can be categorized as in Figure 2: one-way shape (OWSME, Figure 2(a)) and two-ways shape memory effect (TWSME, Figure 2(b)). The former is shown in Figure 1(a), and after recovery and cooling ↔ heating, the material recovers and keeps its non-deformed shape. On the other hand, TWSME allows the material to recovers its non-deformed shape when heated, but returns to the deformed state when cooled back, i.e., at both low and high temperatures the material can remember its shape. This behavior is possible by a heat treatment named ‘training’, where at temperatures in the range of 150-200 °C the alloy is deformed at the desired shape, inducing preferential sites for martensite precipitation and hence directional stresses. Due to these preferential sites, the material is able to recover its previous shape, which was deformed. It is worth noting that OWSME is more beneficial and attractive because it recovers two times more strain that it has to recover by TWSME of the same material [25].

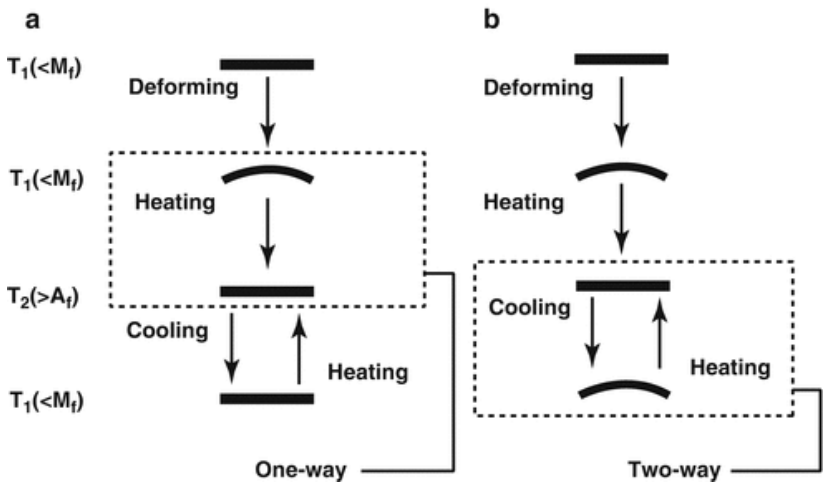

Figure 2. a) one-way and b) two-way shape memory effect [30].

The uniqueness of all these transformations results from the large recoverable strains (up to 10 %), raising significant stresses when the material is sufficiently constrained. The transformation strain can be compared to the ones generated by the standard thermo-elastic behavior, leading to high actuation forces and displacements. For this reason, SMAs are included in the class where piezoelectric and magnetostrictive materials are also comprised [32,33]. Furthermore, as SME occur at a particular temperature, it works both as a sensor and as an actuator. Since the 1990s remarkable developments resulted innovative products. These innovations are based on the aforementioned functionalities and considerable possibilities for functional integration. For this reason, SMAs has been included in “smart” systems with adaptive and/or “intelligent” functions, such as sensors, actuators and micro-controllers [28].

1.1.2 Phase diagram and transformation temperatures

Figure 3 displays the binary Ni-Ti phase diagram. Three are the main classes of NiTi SMA: Ti-rich, equiatomic and Ni-rich. The phases of interest for SMA NiTi are located in the range of 48-56 Ni at.% content, namely, body centered cubic (B2) austenite and monoclinic twined (B19’) martensite. In addition, precipitates also may appear depending on heat treatment and processing conditions, such as Ti_2Ni, $TiNi_3$, Ti_2Ni_3 and Ti_3Ni_4. Trigonal R-phase isb present during the transformation from austenite to martensite B2 → R → B19’, appearing when Ni-rich alloys are i) cold worked and annealed, thus the defects still remain in the matrix and ii) heat treatments precipitate Ti_3Ni_4 that is a precursor of this phase. Orthorhombic (B19) martensite appears when

Ti is partially replaced by Cu, or NiTiCu alloys, and takes place intermediately, i.e. B2 → B19 → B19' [32].

In order to clearly justify the phase transformation mechanisms, it is important to determine the phase transformation terms, these characterized by four transition temperatures: M_f, M_s, A_s, and A_f. From the lowest to the highest temperature, A and M refer to austenite and martensite, respectively, and s and f refers to start and finish. In addition, the limiting temperature for the material to have superelastic behavior (or stress induced martensite) is determined by M_d, and thus above M_d the plastic deformation is permanent [33]. Martensite is stable at temperatures lower than M_f ($T < M_f$) once the transformation from martensite to austenite takes place during heating. On the other hand, at temperatures higher than A_f ($T > A_f$) austenite reaches its stability, since martensite transforms to austenite during heating. Both phases are stable at the temperature between As and Ms.

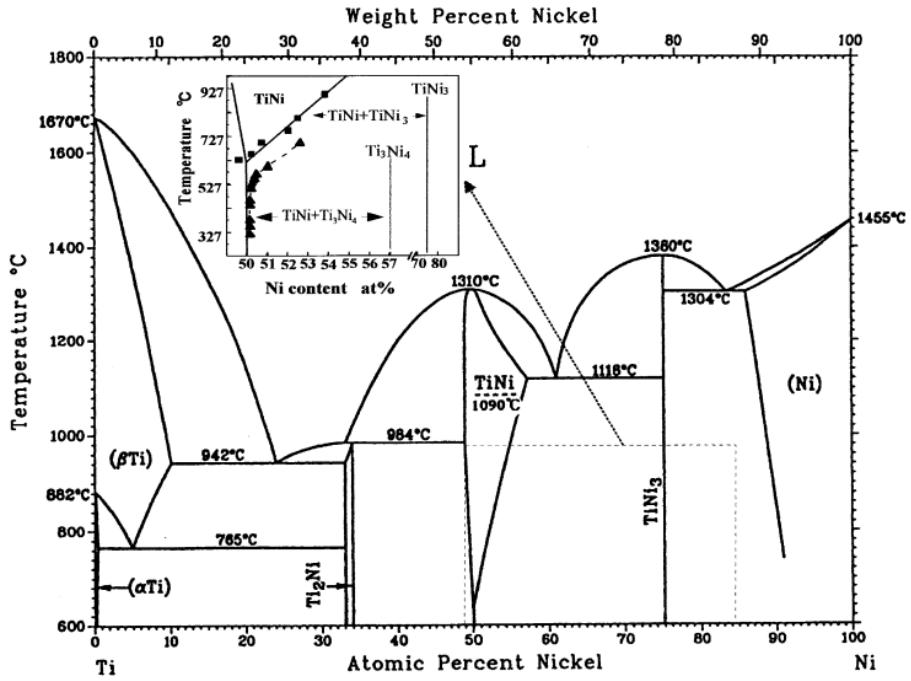

Figure 3. NiTi phase diagram. The insert shows the region of interest for NiTi shape memory alloys [32].

Transformation temperatures plays a major role on shape memory and superelastic effects of NiTi SMA, and these are intimately related to the chemical composition (or Ni:Ti ratio) of the alloy. It is well known that variations in ~0.1% Ni composition shifts the transformation temperature in ~10 °C [34]. Furthermore, not only transformation temperatures but also strength and ductility are very sensitive to impurities such as C,

N and O. Therefore, processing of NiTi has to be carried out as carefully as possible to avoid undesirable fluctuation of composition, hence changes on functional properties, and negative effects of impurity pickups.

One of the most relevant ways for improving the functional properties of SMA is based on heat treatments. For this purpose, the use of Ni-Ti binary phase diagram is of importance, since it indicates which phase and precipitate compose the material under determined conditions of temperature and composition, thus influencing directly on the functional properties.

1.1.3 Manufacturing methods of NiTi

Even though SMAs has successfully established, manufacturing and processing of NiTi is still challenging. Despite such difficulties, several methods have been employed and are summarized in Figure 4. Casting is the most conventional method for producing NiTi. However, the high melting temperature cause undesirable impurities content, such as C, O and N. Increase of impurities leads to the formation of Ti-rich phases, among which TiC and Ti4Ni2Ox, negatively influence NiTi functional properties [7]. Aiming to mitigate or reduce this impurity intake, inert gas is often employed. As-cast NiTi products are not satisfied regarding surface properties and microstructure and thus, in order to achieve a final shape, it needs post-processing activities such as hot/cold working, heat and surface treatments, joining or machining [5,36].

Machining comprises a secondary operation, and is a crucial step to make the final product suitable for applications. However, due to the ductility of NiTi and the strain behavior of the functional effects, machining is still a challenging step. For instance, the strain behavior leads to high tool wear making this process expensive and time consuming. Furthermore, the strain recovery resulting from the functional properties leads to inaccurate final dimensions, thus requiring additional finishing operations. Typically, grinding is a process used for cutting NiTi alloys. Nonetheless, due to high tool wear, laser cutting, photochemical etching, and water jet cutting are good alternatives to get a final product without constraints [5-41].

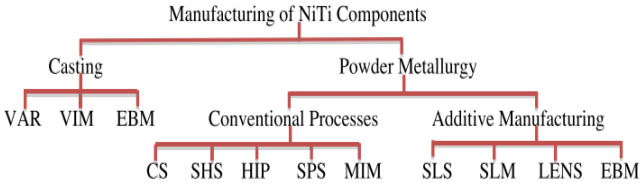

Method	Description	Method	Description
VAR	Vacuum Arc Remelting	SHS	Self-propagating High Temperature Synthesis (combustion) Synthesis
VIM	Vacuum Induction Melting	HIP	Hot Isostatic Pressing
EBM	Electron Beam Melting	SPS	Spark Plasma Sintering
CS	Conventional Sintering	MIM	Metal Injection Molding
SLS	Selective Laser Sintering	LENS	Laser Engineered Net Shaping
SLM	Selective Laser Melting		

Figure 4. Summary of NiTi manufacturing methods [5]

Joining NiTi with dissimilar metal, such as stainless steel, constitutes also a problem. For this purpose, proper interlayer materials are usually required in order to achieve this type of joining. Additionally, similar welding of NiTi is also difficult due to the surface oxide formed between each part, which makes processes such as brazing, fusion welding, and soldering impractical despite possible [5]. Concerning solid state welding, friction stir welding of either austenitic NiTi [36] or NiTi to Al (composite structure) was successfully demonstrated [37].

1.1.4 Additive manufacturing as an alternative technique

The fabrication of a complex part of NiTi has low economic benefits by using conventional methods, and therefore AM is a suitable alternative process. This technique has disrupted as a technological solution to overcome much of the issues revealed by the conventional manufacturing processes presented before. In contrast to conventional subtractive methods, it is based on an incremental layer-by-layer manufacturing where feedstock (powder, wires or sheets) is consolidated into dense 3D objects with the aid of an energy source [4,37,40].

However, the advantages of AM as a fabrication method depends on quantity and complexity of the produced parts, as seen in Figure 5. As stated previously, casting is still the most employed method for fabricating SMA components, irrespective of the fact that secondary operations are required after solidification aiming to reach the desired final shape. On one hand, PM sintering and MIM have shown their capabilities for low and high geometrical complexity, respectively, and large batches, and have been widely employed [26,41,42]. On the other hand, AM has occupied a specific and

competitive niche of fabrication where medium-to-high complexity parts are fabricated in small quantities. It makes AM expensive but not less competitive, since the development of its processes have skyrocketed and thus the benefits have become more attractive.

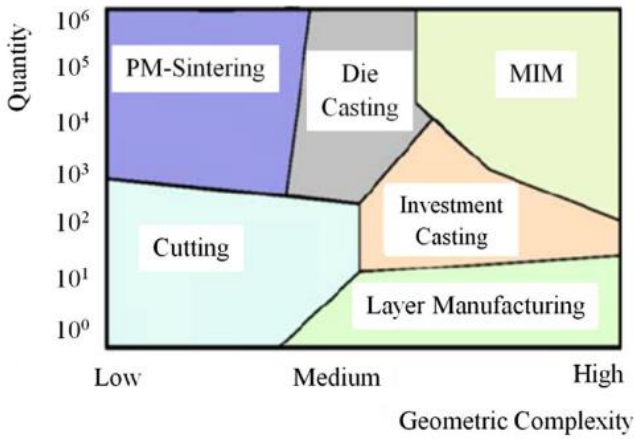

Figure 5. Processing map for metallic materials depending on geometry complexity and quantity. MIM stands for metal injection molding and PM-Sintering powder metallurgy sintering [14].

Concerning AM of SMAs (in this case also including magnetic SMAs), all processes have been employed. Most of the AM of SMA are devoted to powder-bed fusion based processes, most notably selective laser melting (SLM), selective laser sintering (SLS) and electron beam melting (EBM). Moreover, directed energy deposition (DED) processes are broaden employed, being laser engineered net shaping (LENS) often used as a manufacturing way [7].

The biomedical behavior has been extensively reported on AM of NiTi based SMAs due to their potential for a wide array of applications in this field. As it can be seen in recent reviews, SLM is the most employed manufacturing method in this case [7,29,43,44]. According to Dadbakhsh *et al*. one reason for this is the ability to manipulate the stable phase in order to engineer components (e.g. scaffolds). Hence, the shape-memory response and the mechanical properties can be tailored using the laser parameters. The same is valid for the required solid volume fraction or porosity, which are adjusted considering the load-bearing applications of the final implant. Furthermore, since cell proliferation is favorable in regions of smooth curvatures, porous design plays a central role; then powder characteristics and laser parameters are equally important. Therefore, the degrees of freedom provided by AM allows biomedical devices to be designed with maximum biomechanical and physiological

compatibility for a specific patient, reducing the chance of implant rejection, patient healing period, while improving the lifetime performance of the implant [29].

Other than biomedical applications, micro-electromechanical components are also suitable for being fabricated by AM. Following the trend, Clare *et al*. fabricated cantilever beams of NiTi by SLM. The authors showed that the laser power affected the resultant phases in the built component. Consequently, as the power increased, a mixture of martensite and R-phase was identified by means of X-ray diffraction. Interestingly, R-phase is responsible by a gradual phase transition which, in turn, is beneficial for this components' application [46]. Elahinia *et al*. also manufactured a porous SMA actuator by SLM. In this case, this Ti-rich actuator did not require shape settings, since the memorized shape is the printed one. Moreover, besides the simple fabrication method, due to the porous structure the lightweightness was assured [47]. Dudziak *et al*. demonstrated the feasibility of producing micro-actuators by SLS. In this work, fine NiTi powder was processed using SLS aiming to generate structures in the micrometer range. As result the shape memory effect was preserved within a reasonable field of processing parameters, and it was possible to correlate the shift of transition temperature with the process parameters [48].

All in all, powder-based AM processes have been widely studied and successfully employed for producing SMA structures proving the feasibility of powder as a feedstock and both electron beam and laser as energy sources. Nevertheless, up to the moment, few works have been conducted on wire-feed systems where both EBF3 and wire and arc additive manufacturing (WAAM) are located [23,48]. Differently from complex and small sized parts produced by the powder-based techniques, wire-based ones are oriented for larger parts with mid-complexity structures, attaining higher deposition rates and hence higher productivity. Therefore, the opportunities for exploring techniques such as EBF3 are essential and may widen SMA applications, allowing exploring different metallurgical phenomena and capabilities for this kind of alloy.

1.2 Electron Beam Freeform Fabrication (EBF3)

EBF3 has attracted much attention in recent years due to its crucial importance in fabricating near net shape parts resulting important economic benefits. The basic application of the EBF3 process was the electron beam solid freeform fabrication (EBSFF), which was introduced by the U.S. based aerospace company Lockheed

Martin in 1995. A few years later, at the beginning of the 2000's, this process started to be extensively studied and developed by NASA Langley Research Center (LaRC) [50]. It has been demonstrated by these researchers that EBF3 plays a major role in fabricating parts with reduction of costs, waste, and lead-time if compared to traditional manufacturing methods. One has to highlight that EBF3 is a near-net-shape manufacturing method able to fabricate mid-large size parts with medium-complexity geometries. Hence, secondary post-processing methods might be required to achieve the final specification of the parts [49,50].

The main interest of researchers in employing such a processing method was based on its capability to fabricate sparing parts in space or microgravity environment. Aiming to better understand the effects of processing parameters on microstructure and mechanical properties, the researchers published several studies based on statistical analysis [52], microstructural characterization [18], and mechanical assessment [19] showing that parts produced by EBF3 fulfilled the requirements to be employed as structural elements. Therefore, different alloys based on aluminum and titanium started to be produced increasingly showing the potential of EBF3 as a manufacturing process, gradually standing out in the industry (e.g. Sciaky Corp. [53]).

1.2.1. The EBF3 process

Figure 6 illustrates the schematics of EBF3 primary components and operation mode in (a), a deposited structure in (b) and the final product in (c). The process works by introducing a melt wire into a melting pool, which is created and sustained by a focused electron ion beam in a high vacuum chamber. Gradually this substrate is translated with respect to both electron beam and wire and, on each step, the molten metal is deposited over a previous layer until the part reaches near-net shape. By moving in this way, the device enables the structure to be build up, as in Figure 6 (b). Afterwards, if necessary the part undergoes finishing heat treatment and/or machining as in Figure 6 (c) [54].

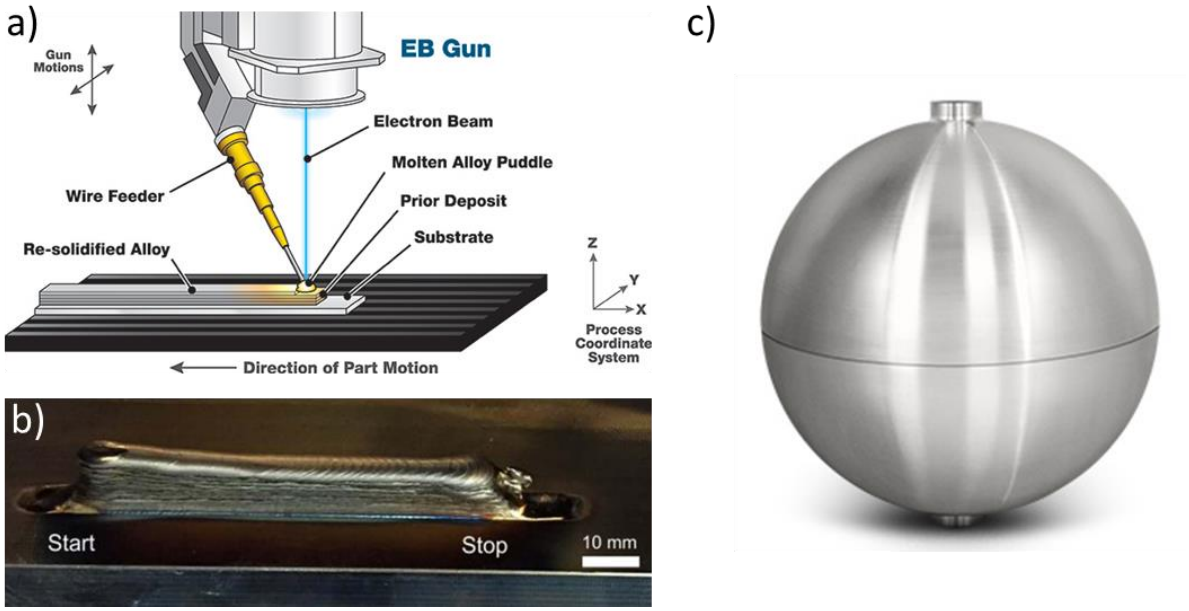

Figure 6. a) Schematic representation of w-EBAM device components [53], in b) material build up at the start in the case of single-directional deposition [54] and c) final product, a titanium propulsion tank from Lockheed Martin [53].

EBF3 process parameters played a key role in the final product properties that are directly influenced by both mechanical properties and microstructure of the part. The main input parameters are accelerating voltage, beam current, wire feed rate, welding speed, and beam focus. The understanding of these process parameters and its interactions ensure the level of quality and certify the process to produce parts for structural applications. Likewise, the relationships between processing-microstructure-property play a key role to support process refinement, leading to, for instance, reduced residual stresses, enhanced surface quality and superior mechanical properties [19]. As an illustration, Figure 7 shows diverse shapes built by EBF3 using Al 2219 aluminum alloy as a feedstock, demonstrating the versatility of the process [55].

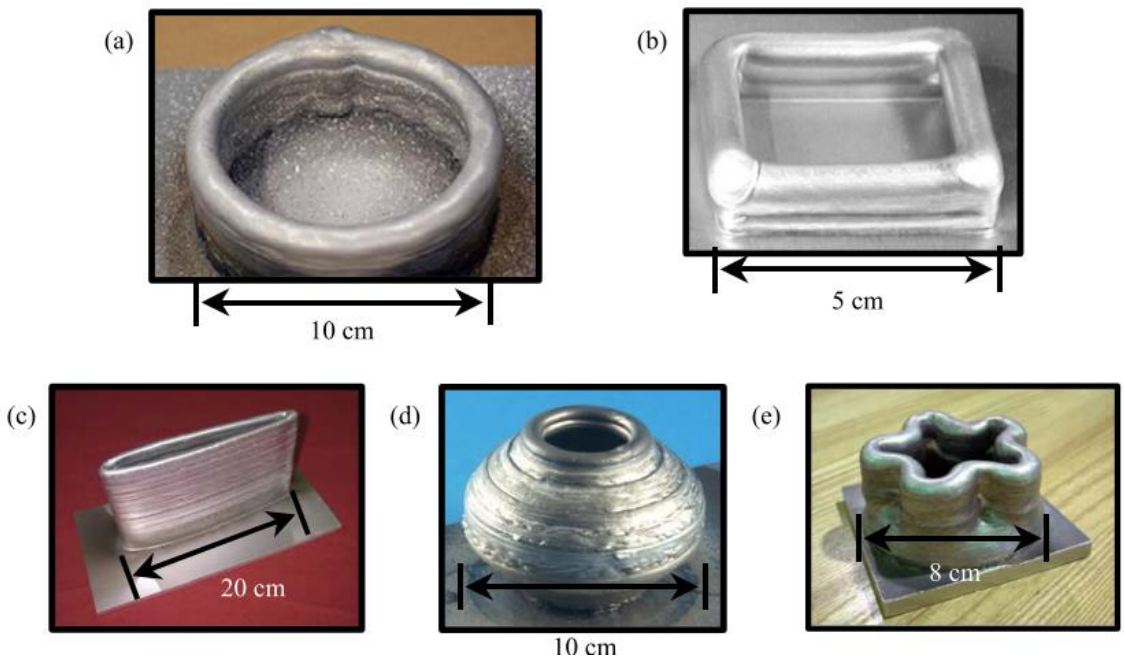

Figure 7. 2219 Al shapes built using EBF3 demonstrate different deposition schemes (a) High deposition rate, (b) varied wire feed angle, (c) complex curvature, (d) unsupported overhangs, (e)transition from one geometry to another [56].

Since EBF3 deposits material in beads, the printed parts are not as finely detailed or as near to net-shape as powder-based AM parts (e.g. produced by SLM). Nonetheless, the finishing is controlled by the wire diameter: fine diameter wires are used if final dimension and surface finish are aimed. On the other hand, when surface finish is not a significant issue and hence post-processing is planned after AM, larger diameter wires are employed – in doing so, higher deposition rates are attained [3,6]. Important improvements were achieved during the maturation of this technology. One can highlight the processing simplicity, comparatively high deposition rates (in excess of 2500 cm^3/hr.), nearly 100% in feedstock consumption and ~95% of efficiency in power conversion [55]. Moreover, as the technology works at ultra-high vacuum the protection against impurities absorption is guaranteed; it is beneficial for processing titanium and aluminum based alloys. But on the other hand, the surplus heat input of EBF3 process caused a couple of limitations. These include a smaller printing resolution due to high deposition rate under high heat input, which restricted the utilization of the process in fabricating low and middle complex parts. Moreover the high heat input leads to high residual stresses and distortion, which resulted in loss of tolerance in the large printed parts, and reduced the quality of surface finish [58]. For this reason, EBF3 has been continuously developed for aerospace fabrication,

including either ground based fabrication of airframe structures or on-orbit construction and repair of space components and structures [2,4].

In overall, EBF3 permits large and semi-complex forms and demands less raw material and finish machining than traditional manufacturing methods. Therefore, it is a potential concurrent to near net-shape forging parts. Forging is applied typically for large aircraft parts – such as pylon, landing gear, fuselage, and wing – made of highly stress-resistant metals, such as titanium, stainless steel and Inconel alloys, requiring complex tooling and dies besides expensive and time taking secondary machining steps. Material input (e.g., bigger billets) and removal by machining is usually very high when producing complex 3D forging parts. Thereby, the buy-to-fly ratio – the ratio referring to the weight of the raw material purchased, compared to the weight of the final part – can be as high as 15-20 for flying components [60]. However, recent publications have reported that parts produced by EBF3 typically shows 50 percent reduction in buy-to-fly when compared to forging, due to less input material, machining steps and lead-time, as well as absence of expensive tooling [60].

1.3 Design of experiments (DoE)

The design of experiments (DoE) is a crucial engineering tool that can be used in order to develop and optimize the process in case of integration with statistics. Analysis of variants, or ANOVA, is considered as a good example of this integration. Over the past of years, both DoE and ANOVA played a major part on, for instance, the optimization the mechanical performance in welding and joining applications by understanding the correlation between the process parameters and the product properties. The main goal behind DoE is to reduce the cost of resources used such as people, materials, time, and equipment. By doing this, data collection becomes more effective since the input variables of the process are better planned. Then, the analysis of this variables and its influences on the responses are more effective [61].

DoE became an attractive tool since it can reduce the manufacturing cost by reducing process design and development time, as well as increase business profitability by reducing defect and scrap rate and retest. In addition, it allows the understanding of the relationship between key process input and outputs [61].

It is worth noting, that DoE has analyzed the responses by separating the process parameters (independent variables) and dependent variables (as a function process parameters). ANOVA is used in order to modify the independent variables and the relevant interaction between a pair of factors. The data gathered from different DoEs

used to predict the impact on the response due to the important process parameters and their interactions, also evaluate the prediction by using the regression equation.

1.3.1 Response surface methodology DoE

Response Surface Methodology, or RSM, is one of the simplest design of experiments method and thus it is mostly used. This technique is based on a set of mathematical and statistical techniques, constituting the functional correlation between input and output variables. The optimization in this method is reached by exploring the surface generated by a 3D representation of response function. The most important response of surface DoEs are the Central Composite Design (CCD) and the Box-Behnken Design, the latter employed in this work [62].

1.3.2 Box-Behnken Design

Box-Behnken Design (BBD) is one of the response surface methodology introduced by Box and Behnken in 1960s. Its design derives from a cube, as seen in Figure 8. It is based on three-level incomplete factorial design, each factor coded in three settings +1 (high-level design), 0 (central point) ,-1 (low-level design), including center and middle points of the edges from the cube [63].

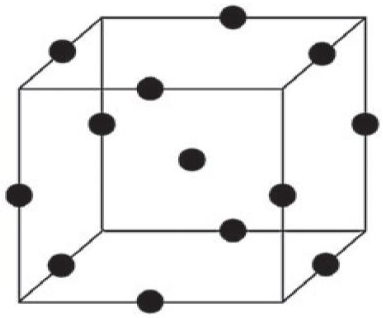

Figure 8. Box-Behnken Design illustrative cube [63].

BBD is considered an economical design, which saves time and costs in comparison with CCB. In addition, this DoE has no corner design points (i.e., extreme runs combining minimum and maximum levels, which can be detrimental to equipment or material), has three-level factorial design, and needs fewer run order. The expression below defines the number of experiments-points (N):

$$N = 2k(k-1) + C_0 \quad (1)$$

where k = number of variables and Co = number of center points.

In the following the response Y is estimated from a nonlinear quadratic model:

$$Y = \beta_0 + \beta_1 x_1 + \beta_2 x_2 + \beta_3 x_3 + \beta_{12} x_1 x_2 + \beta_{13} x_1 x_3 + \beta_{23} x_3 x_3 + \beta_{11} x_1^2 + \beta_{22} x_2^2 + \beta_{33} x_3^2 \quad (2)$$

where Y is the measured output, β_0 the intercept, β_1, β_2 and β_3 linear regression coefficients, β_{12}, β_{13} and $\beta_{23}$the interactive regression coefficient, β_{11}, β_{22} and β_{33} are quadratic regression coefficients, and x_1, x_3, and x_3 the normalized coefficients [64] [65].

BBD is a sufficient design that can be used for RSM due to its built-in serial design, use of blocks and estimative of process parameters in quadratic design, besides the evaluation of the model's lack of fit (LOF). The efficiency of one experimental design as the number of coefficients in the estimated model divided by the number of experiments, demonstrated that BBD is more efficient than three-level full factorial design [65]. Besides, BBD DoEs not consider the design point where all factors are simultaneously in their highest or lowest level. It explains why the vertices of the cube are not covered in BBC, which cause avoidance of experiments under extreme levels and, as a result of that, all the unfavorable factors would not occur [66].

2. Materials and Methods

2.1 NiTi alloy

Both wire and substrate were constituted of NiTi aiming to avoid differences in chemical and physical properties, thus leading to a stable built structure. A 10 mm thick plate was used as a substrate plate (SP) and a 1.2 mm diameter wire as a feedstock, with compositions of Ni50Ti50 and Ni51.2Ti48.8 (at.%), respectively. The composition of both wire and substrate plate were determined by energy-dispersive x-ray spectroscopy in a Tescan Mira3 scanning electron microscope (Dortmund, Germany) at 15 kV. Additional differential scanning calorimetry tests were performed in order to relate such composition to the martensitic starting temperature (since both are intimately related [34]), resulting a good agreement and thus a trustable composition. The substrate plate presented a martensitic starting temperature of 55.3 °C, whereas the wire around -50 °C. In this way, substrate is martensitic at room temperature, whereas the wire is austenitic.

2.2 Electron Beam Freeform Fabrication

EBF3 was conducted on a Pro-Beam EBG45-150 K14 electron-beam welding machine under 5.10^{-4} mbar of pressure. Both accelerating voltage and beam diameter were kept constant during the experimental procedures at 90 kV and 4 mm, respectively, it is worth to noting that the selected voltage (90 kv), which is the minimum accelerating voltage of the device in order to avoid excessive energy density and the possibility of alloying element evaporation / excessive thermal stresses, the further sub-section presents the additional process parameters [66].

2.3 Box-Behnken design of experiment

The process parameters investigated in the present study were welding speed, feeding speed and beam current, and are presented in Table 1. As a response, height and width of ten layer specimens, dilution of single bead depositions, and martensitic starting temperature were evaluated taking into consideration the effect of the aforementioned parameters.

Table 2 show the complete matrix of experiments. Taking into account Equation 1 and the aforementioned parameters, a total 17 runs was performed in which 12 represented single points of BBD and five replicates of the central point. One has to consider that the adopted process parameters range was determined based on

previous wire-based electron beam additive manufacturing procedures, carried out at the same equipment using Ti-based alloys as a feedstock [67].

Table 1. BBD factors and respective variation levels

Factors	Symbol	Levels
Current (mA)	I_S	20, 22.5, and 25
Welding speed (mm/s)	W_s	9, 10.5, and 12
Feeding speed (m/min)	F_s	2.4, 2,85, and 3.3

Table 2. Complete BBD matrix of experiments

Experiment	Factors			Normalized factors		
Order	Is (mA)	Ws (mm/s)	Fs (m/min)	Is	Ws	Fs
R1	22.5	10.5	2.85	0	0	0
R2	22.5	10.5	2.85	0	0	0
R3	22.5	9	3.3	0	-	+
R4	25	12	2.85	+	+	0
R5	25	9	2.85	+	-	0
R6	25	10.5	3.3	+	0	+
R7	20	9	2.85	-	-	0
R8	25	10.5	2.4	+	0	-
R9	22.5	12	2.4	0	+	-
R10	20	10.5	2.4	-	0	-
R11	22.5	10.5	2.85	0	0	0
R12	20	10.5	3.3	-	0	+
R13	22.5	10.5	2.85	0	0	0
R14	22.5	10.5	2.85	0	0	0
R15	20	12	2.85	-	+	0
R16	22.5	9	2.4	0	-	-
R17	22.5	12	3.3	0	+	+

The extension Design of Experiments of Microcalc Origin® software was used to perform data evaluation.

Each of the 17 parameters combinations were deposited in one single bead, five and ten layers stack. Sets of five and ten beads were stacked with a time interval of 30 s

between each layer. All beads were 100 mm long, of which 10 mm was of slope in and slope out – the distance necessary for the parameters to reach its preset values and return to zero, respectively – and 80 mm of steady state deposition, i.e., parameters reach the preset values (or the operative set-up).

2.4 Processing relationships

In order to complement the data resulting from the design of experiments and thus have a more accurate selection of adequate parameters of deposition, a set of equations considering the process parameters are required. These relationships are based on the accelerating voltage (U_B, kV), beam current (I_S, mA), welding speed (W_s, mm/s), feeding speed (F_s, m/min), and wire diameter (d, mm) [68].

In the following, these relationships are given for:

i) Specific energy

$$E = \frac{U_B * I_S}{W_s} \quad [\mathrm{J/mm}] \tag{3}$$

ii) Wire feeding/welding speed ratio

$$\lambda = \frac{F_s * 1000}{W_s * 60} \quad [-] \tag{4}$$

iii) Wire cross-section area

$$A = \frac{d^2 * \pi * \lambda}{4} \quad [\mathrm{mm^2}] \tag{5}$$

iv) Electron beam energy per volume

$$E_V = \frac{U_B * I_S * 4 * 60}{d_{wire}^2 * \pi * F_s * 1000} = \frac{E}{A} \quad [\mathrm{J/mm^3}] \tag{6}$$

v) Deposition rate

$$X = \frac{A * W_s * 3600}{1000} = 15 * \pi * d^2 * F_s \quad [\mathrm{cm^3/h}] \tag{7}$$

Some explanation about the previous equations may help on the interpretation of upcoming results. First, one has to bear in mind that accelerating voltage and wire diameter are keep constant during the depositions in this work. The wire feeding/welding speed ratio (Equation 3) expresses how much of material is fed into the system depending on the welding speed. It means that for a given constant welding speed (Ws), high λ results more material been feed into the system (and vice versa). The electron beam energy per volume (Equation 6), or simply the energy per volume, is the ratio between beam current (Is) and feeding speed (Fs). High energy per volume

means high beam current (Is) or low feeding speeds (Fs) – in contrast, low energy per volume means low beam current or high feeding speeds. Deposition rate (Equation 7) depends exclusively on the feeding speed (Fs).

2.5 Sample preparation

The samples were separated from the substrate plate by water jet cutting. Cross-section NiTi samples were cut by a precision saw, embedded and polished to mirror appearance according to the procedure in Table 3.

Table 3. Sample preparation procedure.

<table>
<tr><th></th><th>Lubricant</th><th>Basis</th><th>Time</th><th>Pressure</th><th>Speed</th><th>Rotation</th></tr>
<tr><td>Grinding</td><td>Water</td><td>Sandpaper</td><td rowspan="2">1 min.</td><td rowspan="2">10 N</td><td rowspan="4">150 rpm</td><td rowspan="2">Co-rotation</td></tr>
<tr><td rowspan="2">Polishing</td><td>9 µm lub.</td><td rowspan="3">Pol. Cloth</td></tr>
<tr><td>1 µm lub.</td><td>10 min.</td><td rowspan="2">15 N</td></tr>
<tr><td>Finishing</td><td>OPS</td><td>30 min.</td><td>Counter</td></tr>
</table>

2.6 Light optical microscopy

Microstructural investigation was carried out using a light optical microscope, LOM (Axio Observer 7, ZEISS, Germany). Measurements of width, height, and dilution were taken from the cross-section of the depositions using ImageJ [69] software. Width and height were measured in ten layers stack specimens, whereas dilution in the one-layer specimens.

2.7 Differential Scanning Calorimetry

Differential scanning calorimetry (DSC) was carried out on a Perkin Elmer DSC 8500 (PerkinElmer, U.S.A.) at 10 °C/min of heating/cooling rate according to ASTM F2004 standard [70]. The analysis started at room temperature, subsequently being cooled down to -50 °C (the lower limit of the equipment), hold for one minute to compensate the thermal inertia, then heated up to 150 °C and hold for the same time; following that the sample was again cooled to -50 °C and the cycle finished. This heating cycle enabled to scan all the transformation peaks related to martensite ↔ austenite phase transformation in the aforementioned interval.

Only the ten layers stack specimens were evaluated. Moreover, the last three to five layers were tested in these specimens, due to the restricted sample diameter (maximum 4 mm) and maximum mass (200 µm) supported by the device.

2.8 X-ray diffraction

X-ray diffraction was executed in a Rigaku Miniflex600 at 25 °C (Rigaku, Japan). The scan speed was of 1°/min in the range of 20 to 120° (2θ), making it possible to detect all the peaks related to the present phases at this temperature. The identification of the peaks was possible by using the software MAUD [71] and corresponding crystallographic information file.

As in the DSC procedure, XRD analysis was performed only for the ten-layer stack specimens. However, differently from DSC, the maximum number of layers were considered in this case. Since the samples were separated from the substrate plate using a precision saw, the first and partially the second layer were removed prior to diffractometric analysis.

2.9 Microhardness

Vickers microhardness was performed in an automated EMCO M1C hardness equipment (EMCO, Austria), where 500 g of load was applied during 10 s (HV0.5 hardness type) to create an indentation. This analysis was performed on ten layer specimens aiming to determine the hardness variation through the layers. Maps with the Vickers microhardness distributions were plotted.

2.10 Dilution

Dilution is the mass of original substrate divided by the sum of combined mass of the substrate and added material melted [72]. Figure 9 illustrates the aforementioned, where Af and Ab stands for area of filler material and of base material.

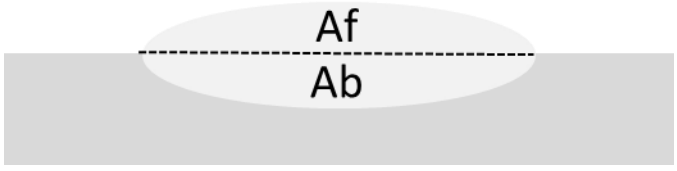

Figure 9. Illustration of dilution

The following relationship is used to determine the percentage of diluted material, or the dilution D:

$$D = \frac{A_b}{A_b + A_f} \quad [\%] \tag{8}$$

2.11 Humping Effect

The humping effect has been intensively studied in the last decades since it limits the attainable welding speed and, therefore, the productivity of several joining technologies such as arc, laser and electron beam welding. When below a critical feeding rate, an ideal situation as depicted in Figure 10(a) is obtained. However, when this limit is surpassed, the formation of ‘drop like piles’ on the top of the weld bead is seen, as in Figure 10(b) [73].

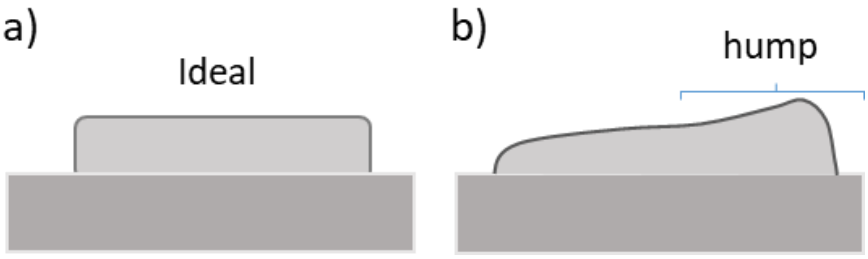

Figure 10. Illustration of a) ideal welding bead and b) humping effect.

Humping depends on statics or dynamics factors such as melt volume, melt flow, and surface tension [74]. Consequently, one has to carefully select the process parameters in order to achieve the balance between welding and feeding speeds, allowing an ideal structure to be built.

3. Results and discussion

The experimental results based on

Table 2 for the responses height, width, dilution and martensitic starting temperature are presented in Table 4. The same table provides the calculations of specific energy (Equation 3), wire feeding/welding speed ratio (Equation 4), wire cross-section area (Equation 5), electron beam energy density (Equation 6), and deposition rate (Equation 7). The aim is to support and simplify the discussions about the influence of each process parameter coupled with data of energy and flux of material.

The following sections are separated in three parts, identified by different colors in the flow chart of Figure 11. The first part, in blue, is devoted to explore how the process parameters variations affected height, width, and dilution (and indirectly martensitic starting temperature). The model equation obtained from the interaction between each process parameter and respective second-order interaction is given on each of these sub-sections, together with the Pareto chart. Aiming to show the reliability of each equation, the actual vs. predicted plot with the validation points – summarized in Table 5 – is presented, followed by the plot of each significant factor for the model equation. The main effect plot is introduced afterwards, in which one can interpret the individual influence of each process parameter on the selected response. Finally, contour plots regarding the interaction between each process parameter are depicted.

The second part, in orange, deals with the selection of optimized process parameter for multitrack deposition. For this purpose, one must adopt criteria concerning surface finishing and geometrical regularity, as well as limits for dilution and martensitic starting temperature, which will be better explained in the coming sections. The last part, in green, introduces the fabrication of multibead tracks based on the selected processing parameters.

Table 4. Running order and respective width, height and dilution values (responses) from the depositions' cross-section as well as the values of wire/welding feeder, specific energy, cross section, energy per volume, and deposition rate from the equations.

Experiment running order	Width (mm)	Height (mm)	Dilution (%)	Martensitic starting temperature (°C)	Wire/welding feeder (-)	Specific Energy (J/mm)	Cross section (mm^2)	Energy per volume (J/mm^3)	Deposition rate (cm^3/h)
R1	5.7	9.9	38	-9.33	4.5	192.9	5.1	37.7	193.3
R2	5.7	10.6	38.5	-19	4.5	192.9	5.1	37.7	193.3
R3	6.1	13.6	33	-40.2	6.1	225.0	6.9	32.6	223.8
R4	5.7	8.5	47	4.58	4.0	187.5	4.5	41.9	193.3
R5	6.8	9.9	47	0.531	5.3	250.0	6.0	41.9	193.3
R6	5.8	10.7	42	-20	5.2	214.3	5.9	36.2	223.8
R7	5.2	11.8	34	-40	5.3	200.0	6.0	33.5	193.3
R8	6.5	7.1	61.5	36	3.8	214.3	4.3	49.8	162.8
R9	5.7	7.3	47.6	7.84	3.3	168.8	3.8	44.8	162.8
R10	5.3	9.1	41.8	-25.3	3.8	171.4	4.3	39.8	162.8
R11	5.3	10.0	38	-17.1	4.5	192.9	5.1	37.7	193.3
R12	4.7	12.8	21.7	-38	5.2	171.4	5.9	29.0	223.8
R13	5.6	9.9	37	-23.4	4.5	192.9	5.1	37.7	193.3
R14	5.3	10.2	39	-22.6	4.5	192.9	5.1	37.7	193.3
R15	4.7	10.4	35.3	-35.73	4.0	150.0	4.5	33.5	193.3
R16	6.2	8.0	45.8	14.8	4.4	225.0	5.0	44.8	162.8
R17	5.2	11.5	31	-31.1	4.6	168.8	5.2	32.6	223.8

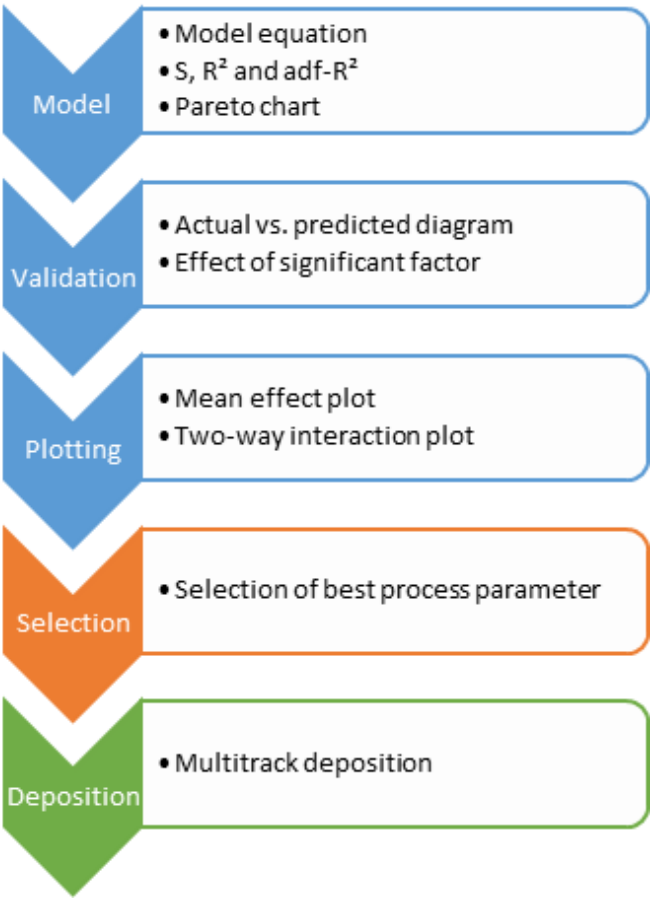

Figure 11. Flow chart of the distribution of results in Results and Discussion section.

Table 5.BBD validation experiments

Experiment Order	Factors		
	Is (mA)	Ws (mm/s)	Vs (m/min)
V1	21	10	2.7
V2	23	10	2.7
V3	23	10	3.1
V4	23	11	3.1

3.1 Box-Behnken Design of experiments of EBF3 of NiTi

3.1.1 Influence of process parameters on height and width

For the height, the obtained model and respective second-order interaction is given by the following equation:

$$Height = -12.2 + 0.27 * BC - 0.17 * WS + 14.24 * FS - 0.0142 * BC^2 + 0.0516 * WS^2 - 0.662 * FS^2 + 0.0027 * BC * WS - 0.018 * BC * FS - 0.504 * WS * FS \quad (9)$$

where beam current is referred as BC, welding speed as WS and feeding speed as FS. Figure 12 shows the Pareto chart of standardized effects, or the effects of the individual factors and its interaction on the bead stacks height. Based on its analysis, FS is statistically the most relevant parameter followed by BC, WS, and the interaction between WS and FS. No quadratic term presented statistical relevance. For this model, S = 0.18, R-squared = 0.97 and adjusted-R^2 = 0.94. Based on these values, one can assert that the model may fit the new data within the experimental range as well as predict new values outside the experimental range.

The actual versus predicted diagram together with the validation points based on Table 5, and the effect of each significant factor are represented in Figure 13. In Figure 13(a) the dotted line described the 1:1 correlation between the axes, and the solid lines enclose the lower and upper prediction limits. One can notice that all the points, from either DoE data or validation points, lied within the confidence interval of 95%. It means that the model for height obtained previously, Equation 9, is trustable for explaining the effect of process parameters on this response. Based on Figure 13(b) it is possible to see that the main contribution of the model comes from FS (73.5%) followed by BC (15.3%) and WS (7.8%), in accordance with the Pareto chart. It was neither a significant contribution from interaction nor from quadratic terms was observed.

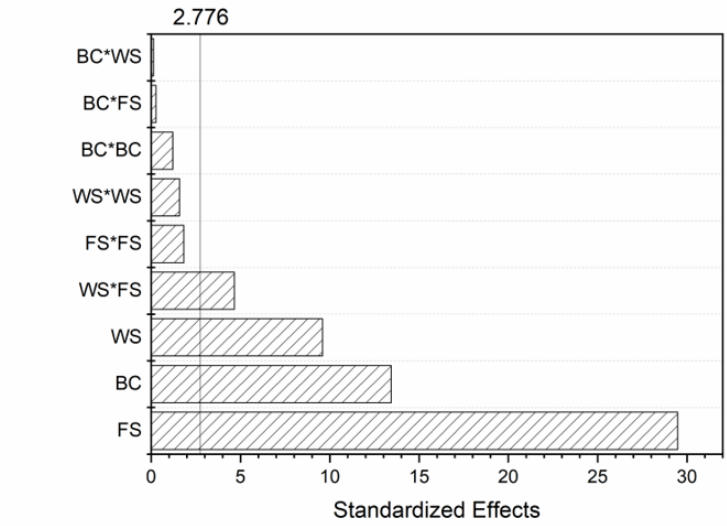

Figure 12. Pareto chart for the standardized effects of the model for height.

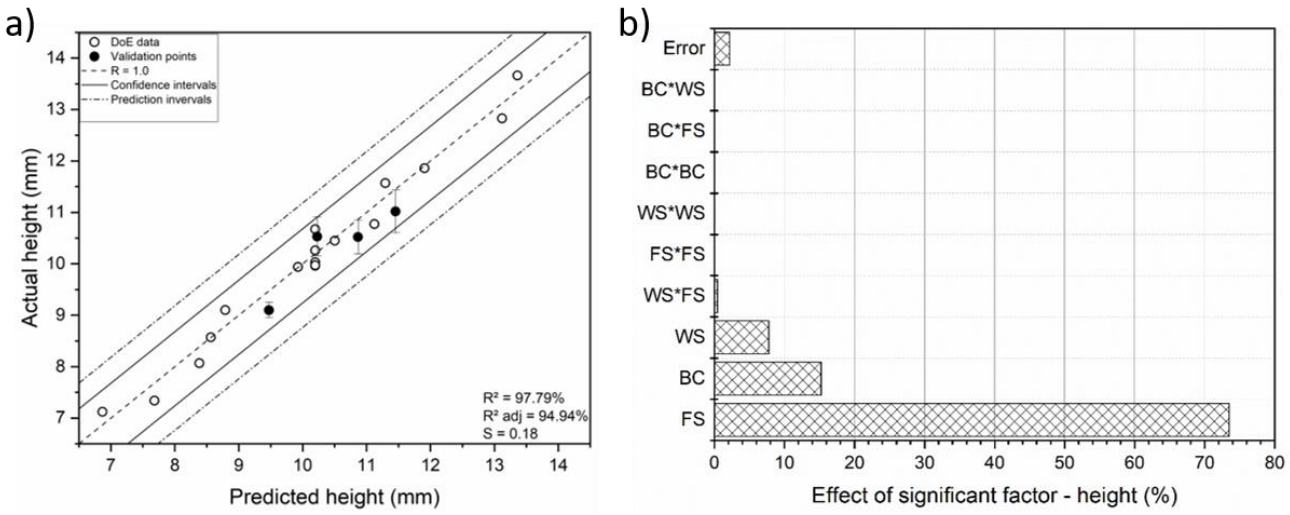

Figure 13. a) Actual versus predicted diagram for the height model and b) percentage effect of each significant factor on the model.

Figure 14 shows in (a) the mean effect plot of height based on the model given by Equation 9. This plot shows the individual contribution of each process parameters related in Table 1. Beam current and welding speed present a negative effect on height, therefore decreasing such response as both increase. In contrast, as feeding speed increases the height also significantly increases, which is in accordance with its major contribution to the model. As a matter of verification, Figure 14(b) shows the micrographs obtained from the cross-sections of each condition with low and high limits for each individual process parameter. One has to highlight that the behavior of height seen in Figure 14(a) is in accordance with previous findings on EBF3 of Ti-64 alloy [52].

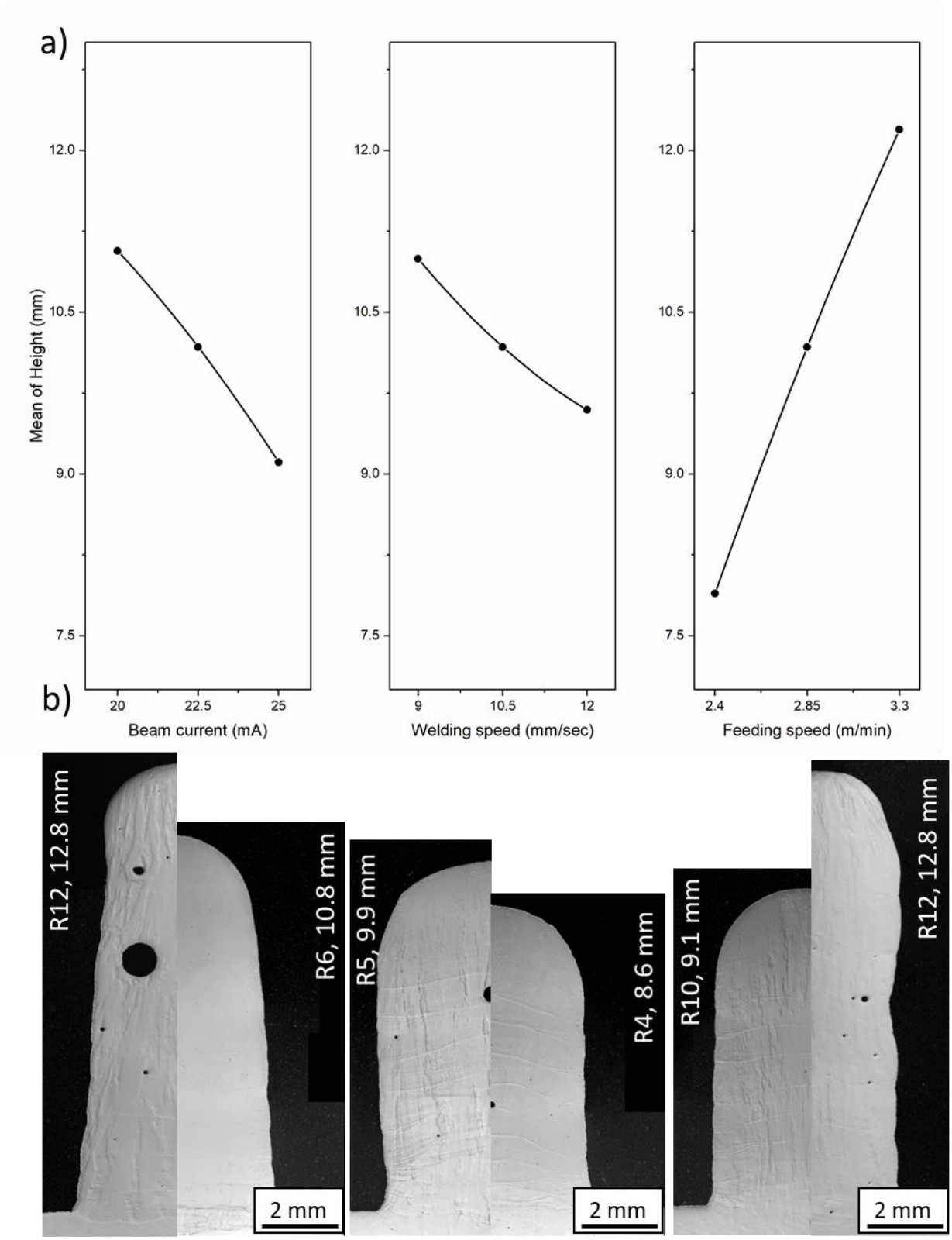

Figure 14. a) Mean effect plot of the process parameters on height and b) selected images of high and low limits of each individual parameter evaluated within the BBD.

When beam current is changed and both welding and feeding speed are kept at the same level, one can notice that, for instance, R12 (20 mA, 10.5 mm/s, 3.3 m/min) is

higher than R6 (25 mA, 10.5 mm/s, 3.3 m/min), as predicted. The role of welding speed is seen when such process parameter varies on its extreme values whereas beam current and feeding speed are in the same level. This situation leads to the comparison between R5 (25 mA, 9 mm/s, 2.85 m/min) and R4 (25 mA, 12 mm/s, 2.85 m/min), where the former is higher than the latter in accordance to the model. Last of all three, the feeding speed is evaluated on its extremes when beam current and feeding speed are in the same level, thus leading to compare R10 (20 mA, 10.5 mm/s, 2.4 m/min) and R12 (20 mA, 10.5 mm/s, 3.3 m/min), finding an improvement on the height.

Figure 15 exhibits the interaction effect between feeding speed, welding speed and beam current for height based on contour plots of the model given by Equation 9. Each contour line represents a constant height in millimeters. The smallest variation in height is observed in Figure 15(a) resulting from the interaction between beam current and welding speed. In this plot, the energy per volume is changing as both variables changes (see Equation 6), despite the deposition rate (Equation 7) is constant since feeding speed DoEs not change (2.85 m/min), resulting 193 cm^3/h. When beam current and welding speed are at its maximum value, 25 mA and 12 mm/sec, respectively, the correspondent energy is 42 J/mm^3 and hence the minimum height is achieved due to a wider molten pool. The opposite, for 20 mA and 9 mm/sec, leads the final height to its maximum, since less energy is employed to melt the same volume of material and therefore one has narrower depositions.

On the other hand, the higher variations seen through this set of plots take place when feeding speed is taking into account, as in Figure 15(b) and (c), due to the major contribution of this term to the model. As a matter of comparison, P1 and P2, both located in Figure 15(b), show the opposite trend for high beam current and low feeding speed (P1) versus low beam current and high feeding speed (P2) – as depicted in Figure 15(d) by the cross-section of each specimen. P1 (7.1 mm high) has the lowest beam current and the highest feeding speed (9 mA, 10.5 mm/sec, 3.3 m/min), the opposite of P2 (9 mA, 10.5 mm/sec, 3.3 m/min). In this condition, P1 has 50 J/mm^3 of energy per volume and 163 cm^3/h of deposition rate whereas P2 (12.8 mm high) has 29 J/mm^3 and 223 cm^3/h for the same parameters. Therefore, one can notice that decreasing energy density and increasing the volume of material feed leads to higher stacks due to narrower melt pools. These values are in accordance to which is proposed by the contour plot, showing once again the reliability of the model given by Equation 9 and therefore of each contour plot.

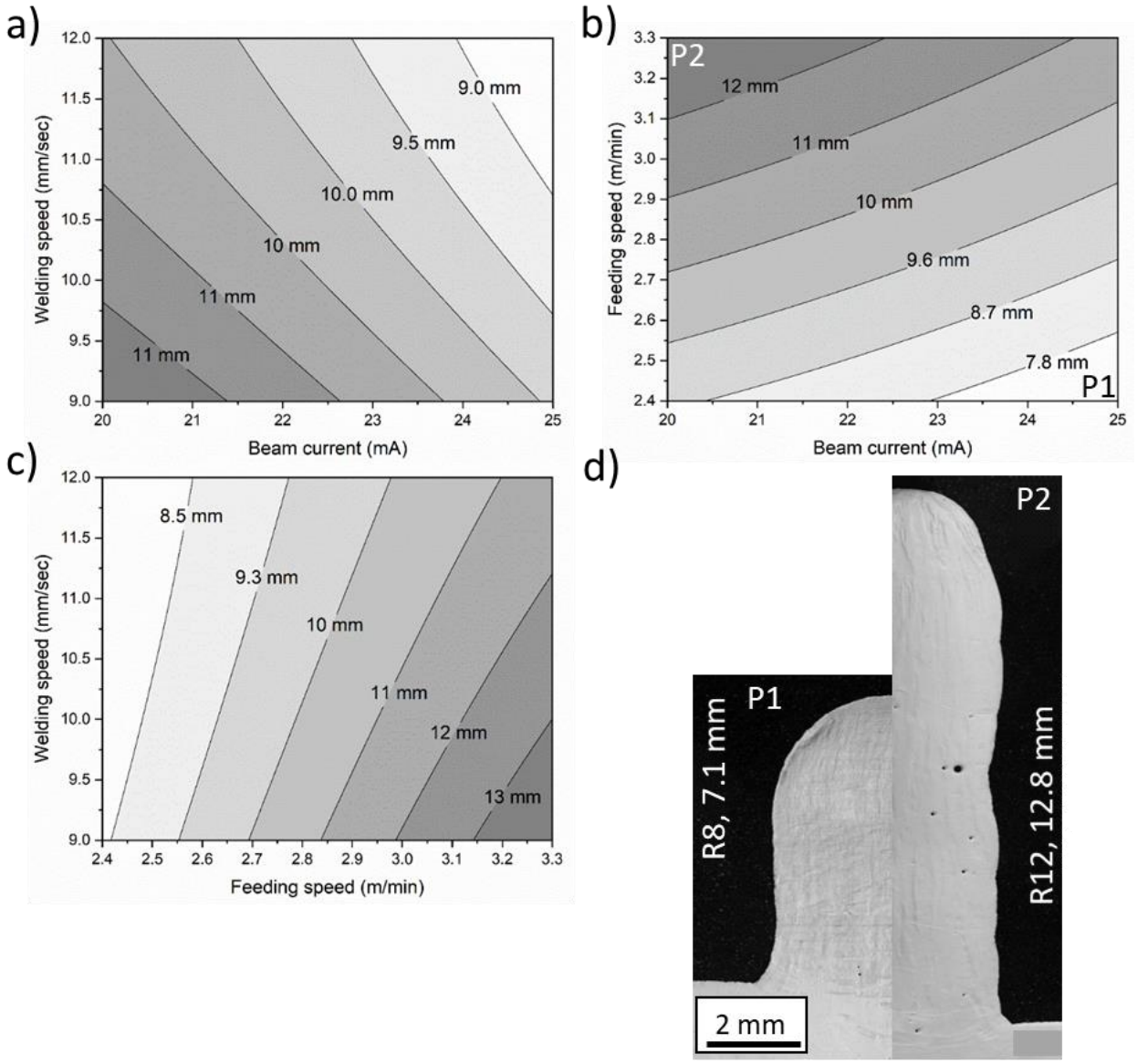

Figure 15. Contour plot of two-way interactions where each contour line is related to height (mm). In (a) welding speed versus beam current, (b) feeding speed versus beam current, and (c) welding speed versus feeding speed. P1 and P2 in (b) are shown in (d), where the cross-section of selected images of high and low limits of each individual parameter evaluated within the BBD.

Concerning the response width, the following model was obtained using the same approach as for the height:

$$Width = -3.8 + 1.257 * BC - 0.30 * WS - 2.65 * FS - 0.0116 * BC^2 + 0.0579 * WS^2 + 0.693 * FS^2 - 0.0387 * BC * WS - 0.0311 * BC * FS - 0.107 * WS * FS \quad (10)$$

The Pareto chart of standardized effects, Figure 16, showed that BC is statistically the most relevant parameter, followed by WS and FS. The interaction between BC and WS as well as the quadratic FS^2 showed itself also relevant. For the model of Equation 10, S = 0.39, R-squared = 0.95 and adjusted-R^2 = 0.84. Therefore, the model may fit the new data within the experimental range as well as predict new values outside the experimental range. Actual versus predicted diagram, the validation points based Table 5, and the effect of each significant factor are represented in Figure 17(a) and (b), respectively.

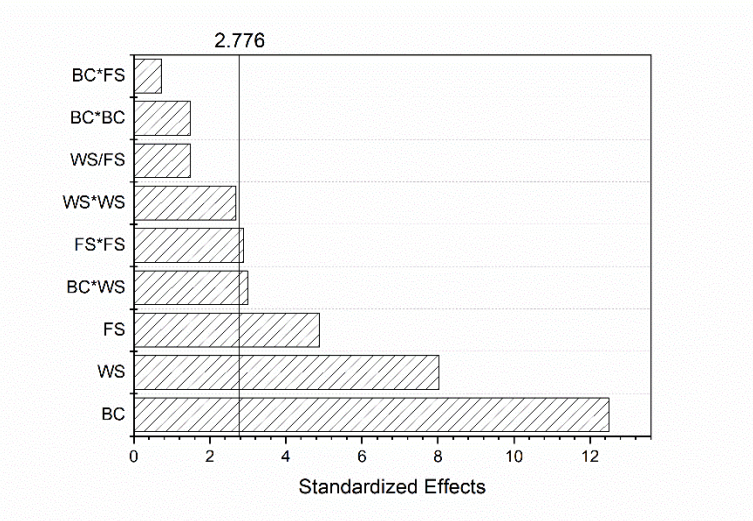

Figure 16. Pareto chart for the standardized effects of the model for height.

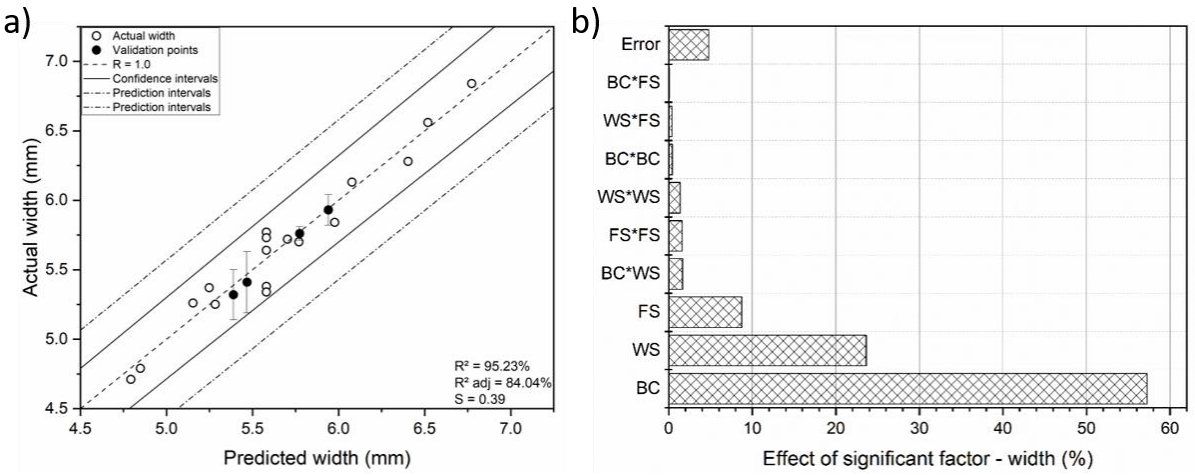

Figure 17. a) Actual versus predicted diagram for the width model and b) effect of each significant factor on the model.

At first, one should highlight that all points seen in Figure 17(a) belonging to both DoE data and validation points are within the interval that comprehends 95% of confidence.

This fact shows that the model for width given by Equation 10 is reliable to explain the mean effect plot. In addition, the contribution of each significant factor, based on Figure 17(b), is as follows: BC (57.5%), WS (23.8%) and FS (9.2%) with minor contributions of the interaction BC*WS (2.1%) and the quadratic ones FS^2 (2.0%) and WS^2 (1.8%).

The main effect plot based on the model given by Equation 10 and the cross section images of each 10 layers stack corresponding the extremes for beam current, welding speed and feeding speed are in Figure 18(a) and (b), respectively.

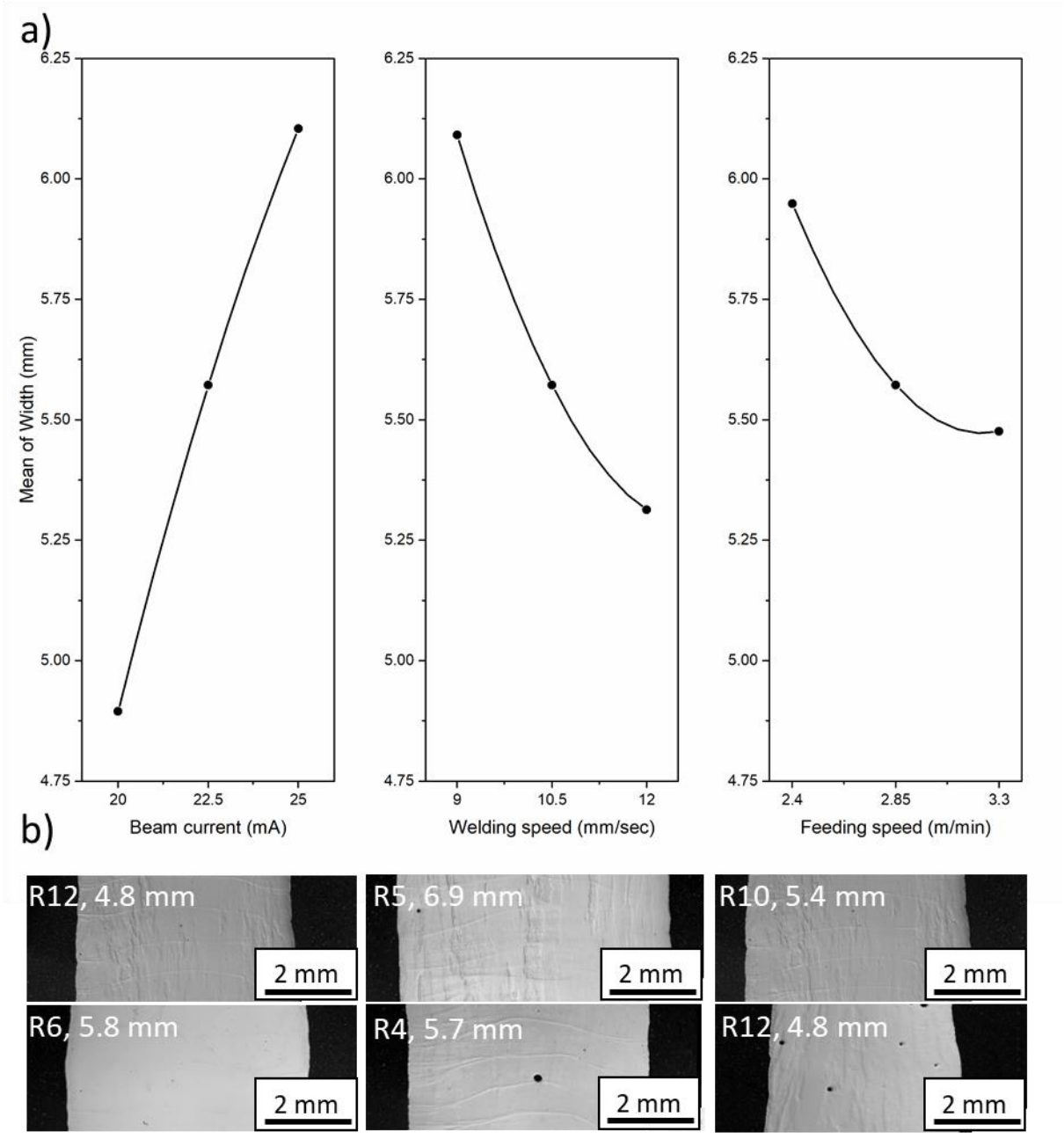

Figure 18. a) Mean effect plot of the process parameters on width and b) selected images of high and low limits of each individual parameter evaluated within the BBD.

One can notice a negative effect of welding and feeding speed on width, meaning that if beam current is keep at a constant value and both are increased the resultant width is reduced. Conversely, beam current has positive effect on the width. This behavior corroborate the findings of Wallace *et al*. [52].The interaction plots between each of the process parameters are displayed in Figure 19. Each of the lines represent width in millimeter, and all plots were based on Equation 10. The largest variations are found in Figure 19 (a) in reason of the major contributions of beam current and welding speed to the model. Following, beam current versus feeding speed and welding speed versus feeding speed also present variations when the contour lines are transposed, but into a lesser extent. In a practical way, Figure 19(d) shows the cross-section of ten layer depositions of P1 in Figure 19(b) representing R8 (25 mA, 10.5 mm/s, 2.4 m/min) is 6.5 mm wide and P2 in Figure 19(a), where R15 (20 mA, 12 mm/s, 2.85 m/min) is 4.7 mm wide. Since the mass conservation principle is applied during the deposition, i.e., losses in height become additions in width and vice versa, the same explanation for the variations observed in Figure 15 may be applied to justify the ones observed in Figure 19. Last but not least, despite of a small difference between predicted and measured values, the latter are in excellent agreement with the model proposed by Equation 10.

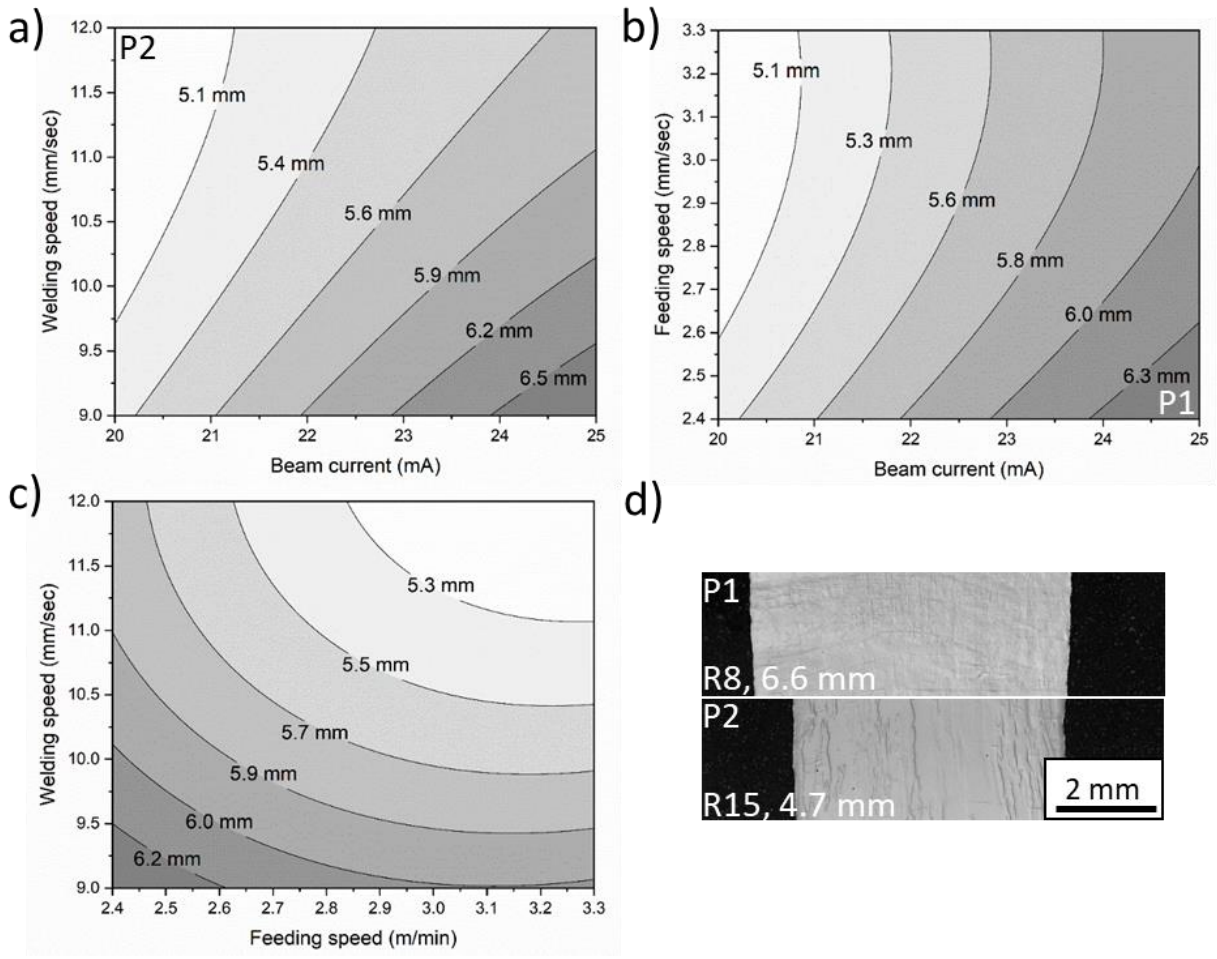

Figure 19. Contour plot of two-way interactions where each contour line is related to width (mm). In (a) welding speed versus beam current, (b) feeding speed versus beam current, and (c) welding speed versus feeding speed. P1 in (b) and P2 in (a) are the cross-section of selected images of high and low limits of each individual parameter evaluated within the BBD.

3.1.2 Influence of process parameters on dilution and martensitic starting temperature

The same approach of the previous section is used to explain the effect of process parameters on the responses dilution and martensitic starting temperature (Ms). Nonetheless, the behavior of both responses are linearly correlated and follow the same trend, as seen Figure 20. For the range of energy adopted during the depositions, one can see that both dilution and Ms increases linearly in a strong relation proved by the adjusted R^2: 0.91 for dilution and 0.89 for Ms. Therefore, dilution is selected in this thesis to describe the effect of process parameter on it. Additional data related to Ms is provided in Appendix.

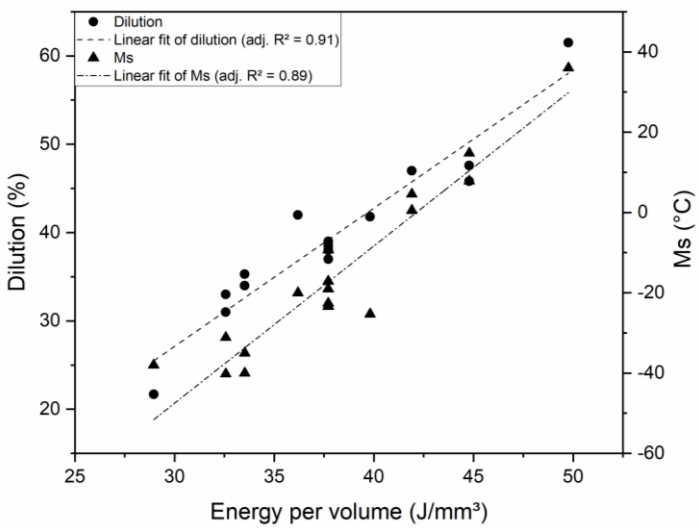

Figure 20. Dilution and martensitic starting temperature (Ms) in function of energy per volume.

The model for dilution based on statistical analysis is given in the following equation:

$$Dilution = 2.24 - 0.147*BC + 0.045*WS - 0.380*FS + 0.00410*BC^2 + 0.00072*WS^2 + 0.0537*FS^2 - 0.00087*BC*WS + 0.0013*BC*FS - 0.0141*WS*FS \quad (11)$$

The Pareto chart in Figure 21 depicts the major relevance of FS and BC. BC² shows its importance as third, followed by FS² and the interaction WS*FS. Interestingly and differently from height and width, the model provided by Equation 11 has more relevance of the terms BC, FS, 11and related interactions, and a negligible impact of WS. The values of S = 0.02, R² = 0.96 and adjusted-R² = 0.91 address a model that may fit experimental and new data within the experimental range.

The actual versus predicted diagram, the validation points based on Table 5, and the effect of each significant factor are presented in Figure 22(a) and (b), respectively. The good fitting of the model given by Equation 11 is seen in Figure 22(a), since all the points - either belonging to the DoE data or validation points -, are located within the interval of confidence. The weight of FS (49%) and BC (43.6%) are evident for the model in Figure 22(b), and a small influence of BC² (2.4%) is noticed; no effect of WS is observed.

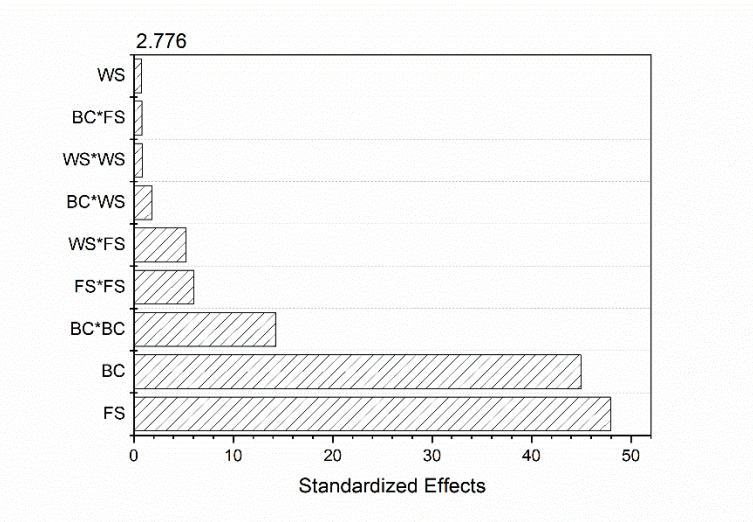

Figure 21. Pareto chart for the standardized effects of the model for dilution.

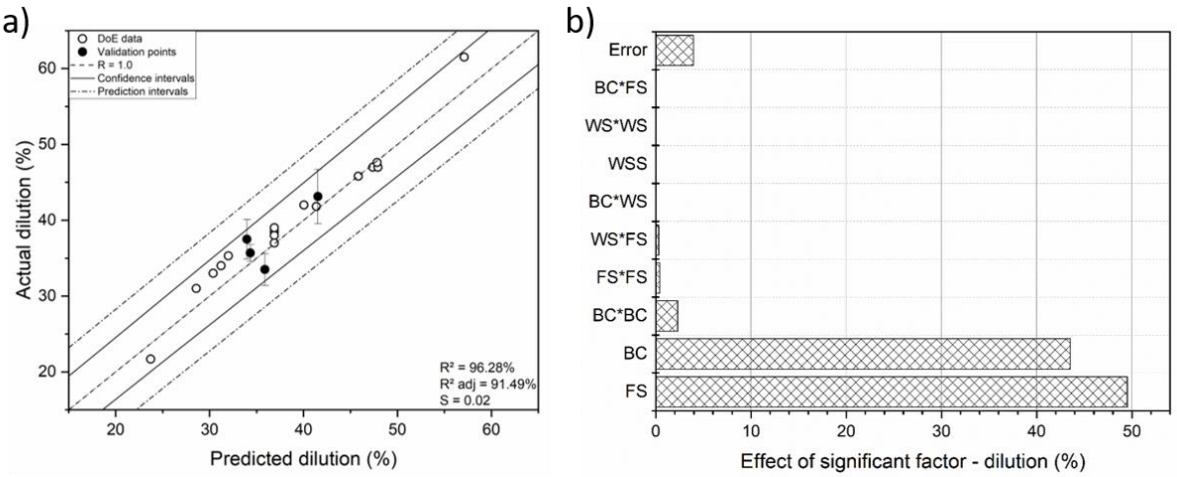

Figure 22. a) Actual versus predicted diagram for the width model and b) effect of each significant factor on the model.

The described behavior reflects directly on the main effect plots in Figure 23(a), all based on Equation 11. The relevance of both beam current and feeding speed are clearly visible due to its steep lines. On the other hand, welding speed shows a horizontal profile resulting from its irrelevant influence. Focusing on the cross-section seen in Figure 23(b), the comparison between R12 (25 mA, 10.5 mm/s, 3.3 m/min) and R6 (20 mA, 10.5 mm/s, 3.3 m/min) shows that by varying beam current from 20 to 25 mA it is possible to reach almost the double of dilution; from 21.7 to 42.0%. For feeding speed, the trend is opposite nonetheless identical: R10 (25 mA, 10.5 mm/s, 2.4 m/min) has twice the dilution of R12 (25 mA, 10.5 mm/s, 3.3 m/min). As mentioned, the dilution keeps the same value when welding speed change into its extreme values

between R5 (25 mA, 10.5 mm/s, 3.3 m/min) and R4 (25 mA, 12 mm/s, 2.85 m/min): 47%. Regarding Ms, it follows exactly the same trend as for dilution, i.e., no influence of WS and expressive variations of the transformation temperature when both beam current and feeding speed are changed between extremes.

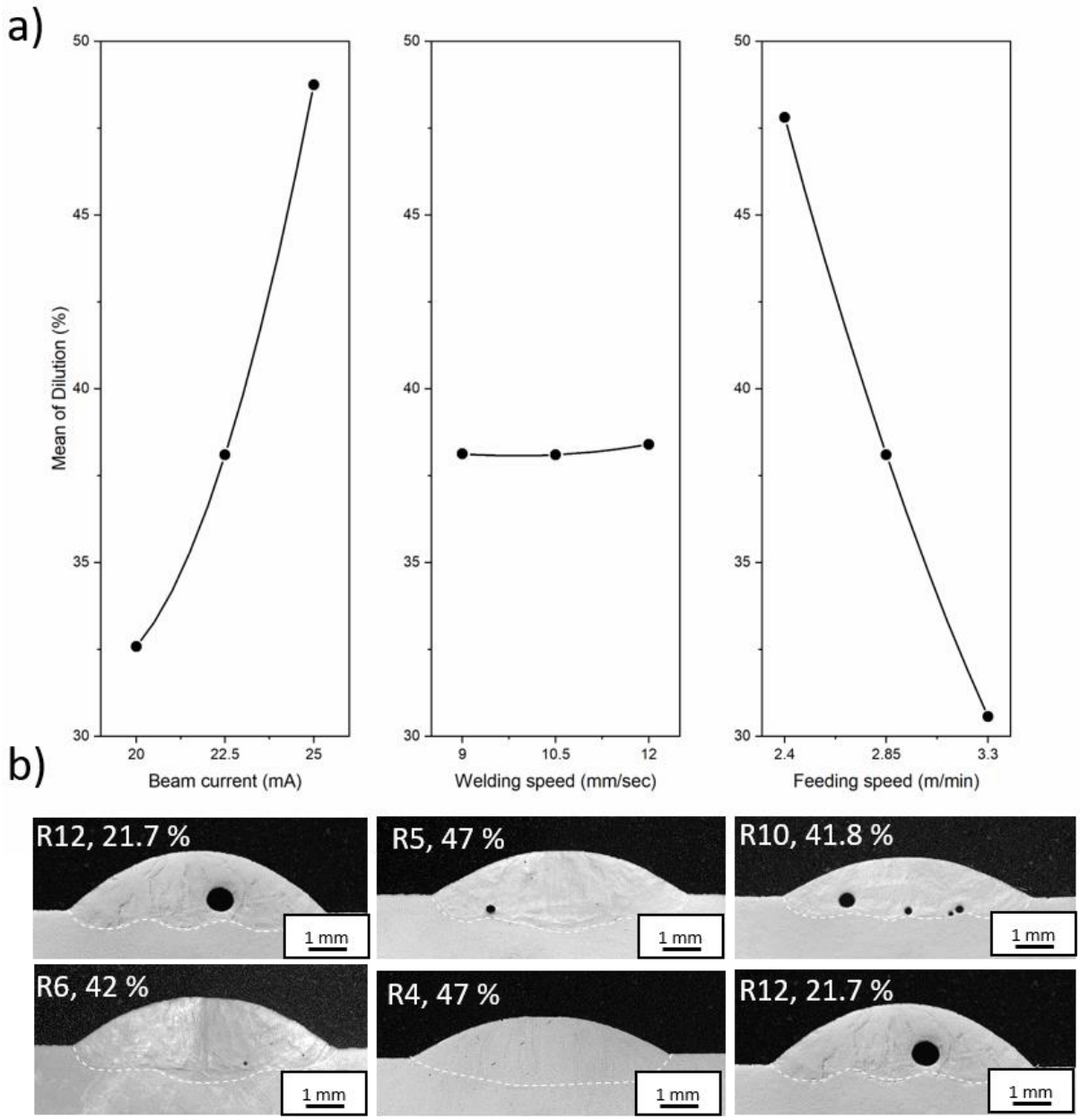

Figure 23. a) Mean effect plot of the process parameters on dilution and b) selected images of high and low limits of each individual parameter evaluated within the BBD.

The interaction plots based on Equation 11 are displayed in Figure 24, where each of the contour lines represent the dilution in %. In Figure 24(a) the changes in dilution are expected only to take place when the beam current changes, varying

perpendicular to the contour lines. However, when welding speed varies at a certain beam current dilution tends to be constant. In terms of mass and energy flux: for a given beam current, when welding speed increases the specific energy (E, Equation 3), the ratio wire feeding/welding speed (λ, Equation 4), and the wire cross section area (A, Equation 5) decreases proportionally. It keeps the energy per volume (Ev, Equation 6) constant and since the deposition rate (X, Equation 7) is constant, the same amount of energy is spend to melt the same volume of material on this contour line, and for this reason the dilution is invariant. Through the lines, the variation of beam current changes the energy per volume, and therefore one has different values of dilution when welding speed is constant.

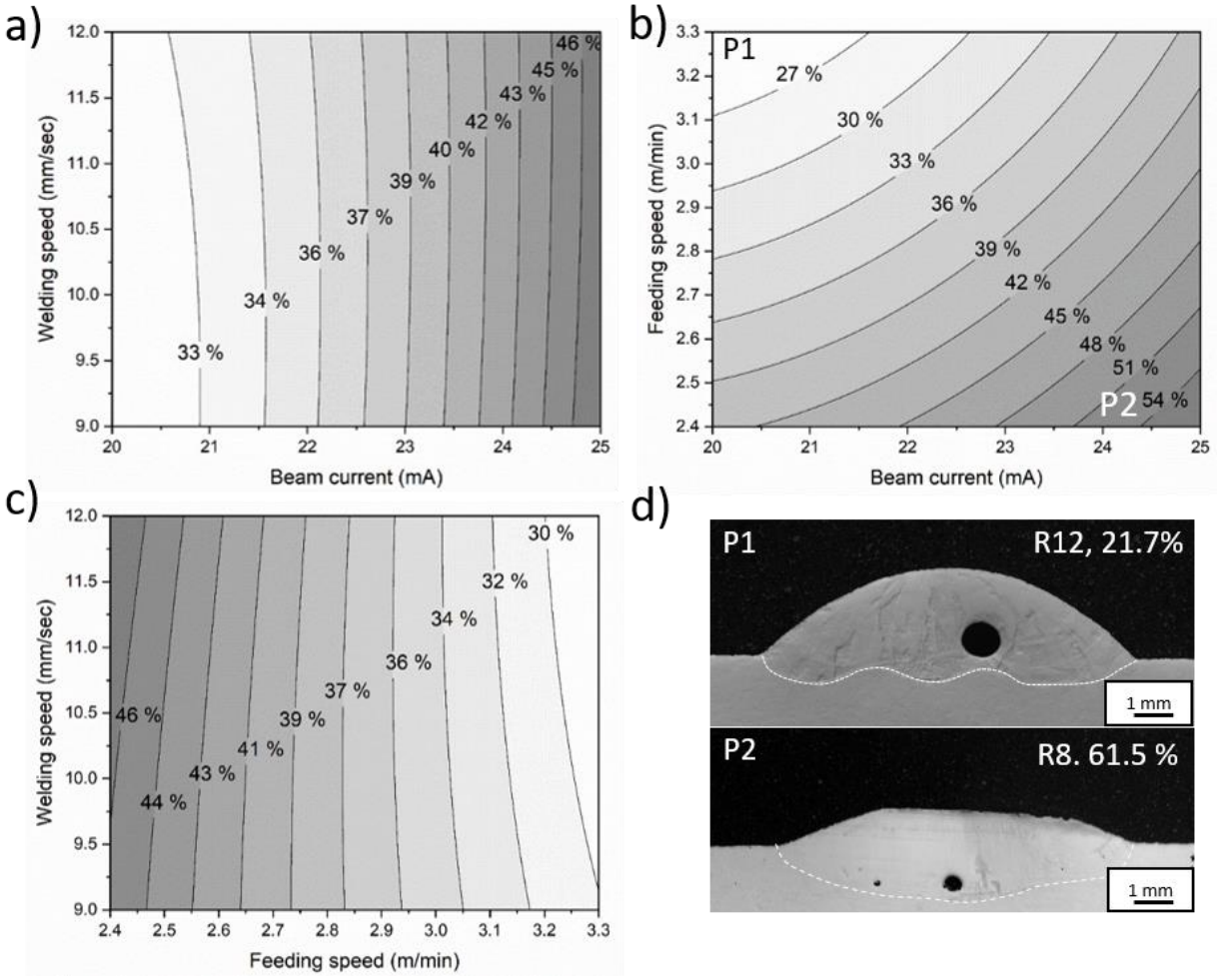

Figure 24. Contour plot of two-way interactions where each contour line is related to dilution (%). In (a) welding speed versus beam current, (b) feeding speed versus beam current, and (c) welding speed versus feeding speed. P1 in (b) and P2 in (a) are the cross-section of selected images of high and low limits of each individual parameter evaluated within the BBD.

In Figure 24(c) if feeding speed is changed, so DoEs the deposition rate. For a given feeding speed, the variation of welding speed has the same effect as in Figure 24(a), and thus dilution is constant along the contour lines. On the other hand, for a certain welding speed and if the feeding speed increases, the ratio wire feeding/welding speed λ, the wire cross section area A, and the deposition rate X increases proportionally. Nonetheless, the specific energy Ej remains constant and thus the energy per volume Ev decreases. In other words, by increasing feeding speed in Figure 24(c) the flux of material increases and the energy for melting it decreases. Hence, less energy flows through the substrate plate, thereby reaching a lower dilution.

Figure 24(b) shows a strong interaction between both beam current and feeding speed. P1, representing R12 (20 mA, 10.5 mm/s, 3.3 m/min), and P2 R8 (25 mA, 10.5 mm/s, 2.4 m/min) depict the extreme cases of beam current and feeding speed; their cross-sections are given in Figure 24(d). Noticeable variations in dilution occur when going from P1 to P2, where low beam current and high feeding speed causes 21.7% (P1) and high beam current and low feeding speed lead to 61.5% (P2) of dilution. One can explain this improvement by remarkable differences found on these corners concerning energy per volume and deposition rate. P1 has high deposition rate (223 cm^3/h) and low energy per volume (29 J/mm^3), whereas P2 has the opposite: 163 cm^3/h and 50 J/mm^3. Higher volume of wire material is molten by a lower energy density beam in P1, gradually changing the scenario to lower volume of wire material molten by higher energy density beam in P2. It leads to more energy flowing from the molten wire material through the substrate plate, and hence widening the melting pool increasing dilution. Apart from this improvement, one has to take into account the identical behavior faced by Ms: not only dilution increases from P1 to P2, but also MS (as indicated in Figure 20). This can be explained by the excessive energy per volume that also contributes to evaporate Ni in the wire. Therefore, a two-way phenomenon is observed here: increasing dilution also indicates variations on the chemical composition of the alloy due to Ms variations. For this reason, both have to be avoided during the selection of best processing parameter.

3.2 Selection of the optimized process parameters

Once the range of parameters was not wide enough to capture points of maxima and minima, establishing optimized values was not possible. For this reason, the BBD was relevant to understand the influence of beam current, feeding and welding speed on

height, width and dilution (and indirectly on the martensitic starting temperature) showing some trends to be followed during the screening.

3.2.1 Selection of adequate deposition parameters based on individual contributions of energy per volume, dilution and Ms

The screening of process parameters aiming to find the optimized set is based on some requirements. Firstly, one should employ the lowest energy level to avoid excessive dilution, Ni evaporation, and impurity pickup. By considering it, the beam energy is employed to melt the wire effectively, directing less energy to flow through the substrate plate – hence lower energy losses are attained and less thermal stresses are induced into the substrate plate –, and the chemical composition of the deposition remains as close as possible of the wire, i.e., the deposited alloy keeps its properties. This approach is frequently used for the determination of optimized processing parameters in powder based AM [11,72,73].

When these requirements are fixed, the Table 6 shows the running orders may be pre-selected as potential optimized sets:

Table 6. The better five candidates running conditions

Candidate	Beam Current (mA)	Welding Speed (mm/s)	Feeding Speed (m/min)	Energy Density (J/mm³)	Dilution %	Ms temperature C°
R3	22.5	9	3.3	32.6	33	-40
R7	20	9	2.85	33.5	34	-40
R12	20	10.5	3.3	30	35.3	-38
R 15	20	12	2.85	33.5	35.3	-35
R 17	22.5	12	3.3	32.6	31	-31

The five aforementioned selected conditions were considered for a further screening based on deposition regularity and quality.

3.2.2 Selection based on surface regularity

One has to consider structural factors, and hence a second step of the screening consists on the evaluation of surface regularity. For this purpose, the evaluation of cross-sections of ten stacks depositions (or 10L) is necessary, and this set is depicted

in Figure 25. At first sight, one can notice that R12 is discarded due to its irregular surface (highlighted by the white dashed lines). This might result from excessive height to width ratio, since the stacking becomes irregular with remarkable differences in width resulting the grooves. On the other hand, all other candidates are suitable, despite the visible porosity, a common feature in EBF3 [77] and other AM processes.

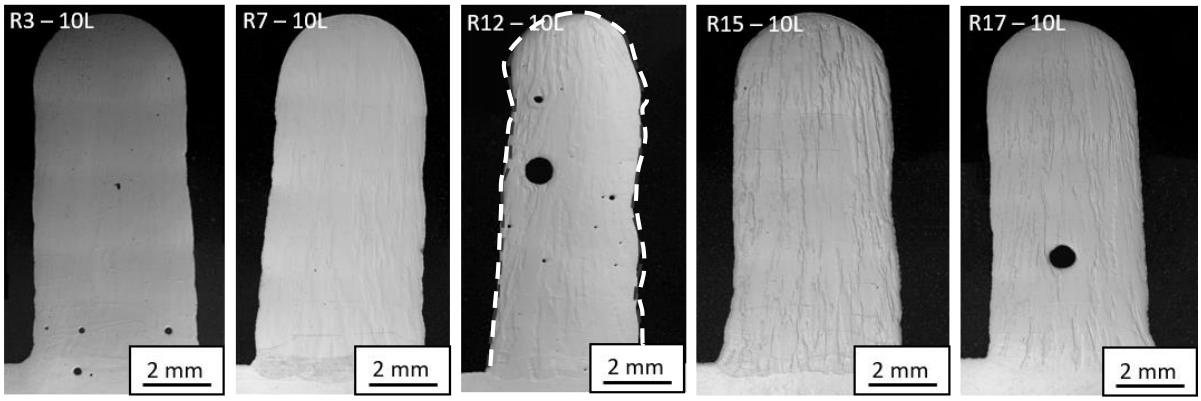

Figure 25. Cross-section views of R3, R7, R12, R17 and R15. The white dashed line in R12 highlights the irregular surface.

3.2.3 Selection based on the humping effect

Another effective screening parameter constitutes the humping effect. It results from the combination of lower currents and relatively higher welding speeds. When beam current is sufficiently low, the hump becomes more pronounced and differences in height are verified in the same deposition. Humping compromises both quality and homogeneity of the part and hence also the process productivity, since higher welding speeds are not possible due to such deleterious effect [78]. In Figure 26 the white dashed line contours the humps on each of the four conditions. It is interesting to notice that despite the same welding speed (9 mm/sec), R3 (22.5 mA) has higher beam current than R7 (25 mA) and hence the effect is less pronounced; this improvement in energy is used to remedy the effect and is widely employed strategy to reduce humping [74]. Nonetheless, one should ideally eliminate both parametrical limitations to reduce or eliminate humping. R15 and R17 present very low humps and; furthermore, the layers seem to be deposited regularly, leading to a better surface quality. For this reason, both are considered for the next step.

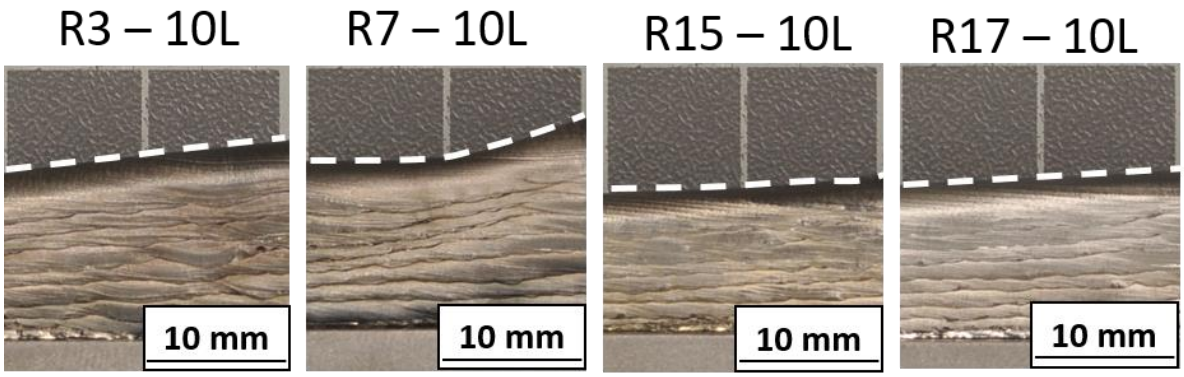

Figure 26. Evaluation of the deposition regularity on R3, R7, R15 and R17.

3.2.4 Final selection

The last step comprehends the selection between R15 and R17. The comparison considering energy per volume and deposition rate (processing aspects), as well as dilution and Ms (processing effects) of both conditions it displayed in Table 7. R15 has a slightly lower Ms if compared to R17, while the latter takes a short advantage on both lower energy per volume (Ev) and dilution. However, since R17 has a higher feeding speed than R15 (3.3 and 2.85 m/min, respectively), it delivers a higher deposition rate and thus presents a higher productivity. Since aspects such as dilution, Ms, and surface quality are satisfactory for this condition, R17 was finally selected as the optimum process parameter for further multitrack deposition.

Table 7. comparison between R15 and R17

Condition	Ev (J/mm³)	Dep. Rate (cm³/h)	Dilution (%)	Ms (°C)
R15	33.5	193.3	35.3	-35.7
R17	32.6	223.8	31	-31.1

3.2.5 Characterization of optimal processing parameter

Once the selection of best processing parameter is finished, a basic characterization of the ten-layer deposition is required. Figure 27 depicts the complete cycle of DSC that defined Ms. It shows endothermic and exothermic peaks denoting the austenite ↔ martensite (M ↔ A) transformation, respectively, implying the occurrence of phase transformation upon heating and cooling. Hence, the shape memory effect correlated to this reversible transformation is present on this deposition. Furthermore, since R17

is austenitic at room temperature, it is possible to assess mechanically the superelastic effect without additional heating or cooling steps. Therefore, the as-fabricated state of the selected deposition parameter presents functional properties. Further heat treatments are required to improve the functional behavior as well as chemically homogenize the deposition [8,33,76], and will be addressed in the future.

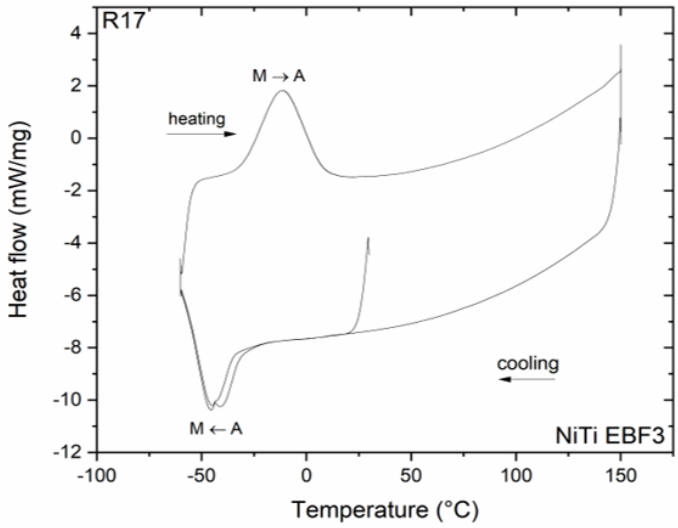

Figure 27. Differential scanning calorimetry of ten layered R17 condition, where M and A stand for martensite and austenite, respectively.

Figure 28 shows the XRD analysis of R17, aiming to identify the phases present in the selected condition. At first, one can notice the background contribution from the equipment, an effect of the small sample size. Nonetheless, the peak identification was possible irrespective of this artifact. A matrix mostly composed by austenite (or B2 long order phase) can be observed, along with few and low intensity peaks of Ti_2Ni, a Ti-rich particle that precipitates during the processing. The same was observed in a Ni-rich alloy deposited via plasma arc deposition, with implications on the superelastic effect [80].

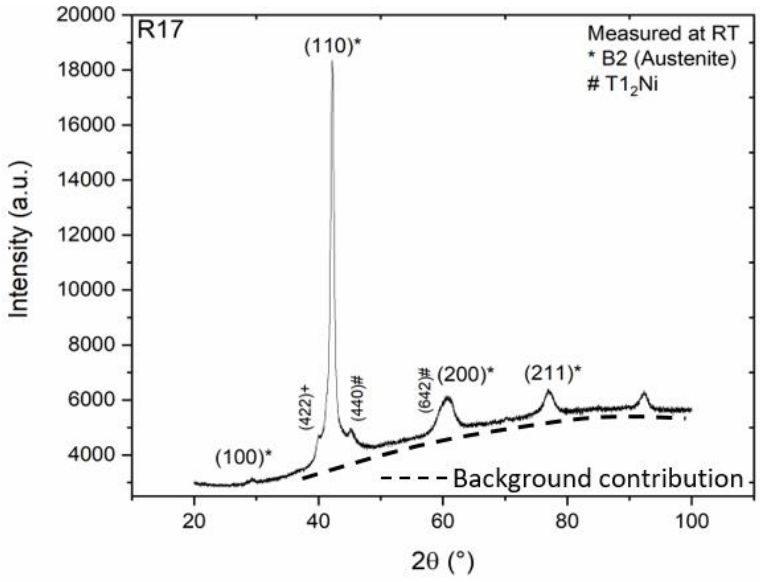

Figure 28. X-ray diffraction of R17 condition.

The hardness profile in Figure 29 highlights the differences between martensite – predominant on the substrate plate**,** on the first and partially on the second layer – and austenite, from the second layer on [81]. The first layers suffer from Ni-depletion both resulting from the evaporation of such element and from the dilution, since one has to feed the melting pool in the substrate with the wire to sustain the process. From the first layer to the second the dilution vanishes out, and hence the Ni amount increases. This improvement influences directly Ms, and therefore one observes a transition at room temperature from martensite to austenite. Considering from the third layer on, the hardness ranged from 260 to 360 HV. If compared to the literature, it is possible to find values from 290 HV (Ni50.8Ti49.2 processed by SLM [76]) to 600 HV (Ni53.5Ti46.5 processed by wire-arc [82]). Therefore, this property is in the expected range for additive manufactured NiTi SMAs.

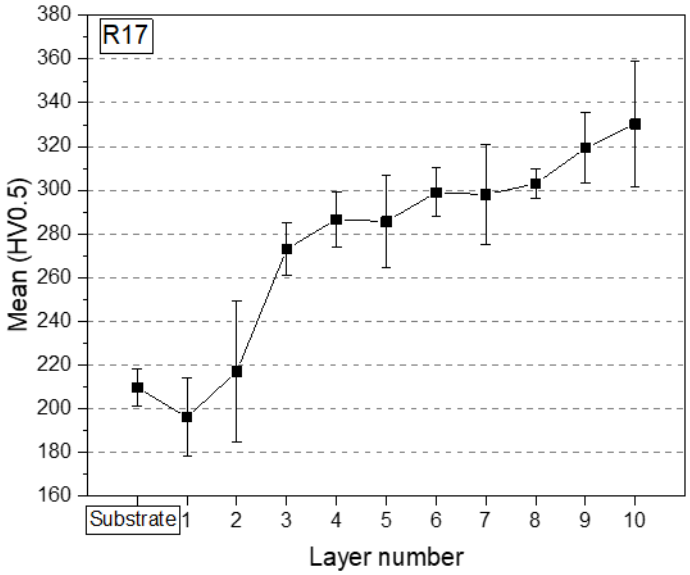

Figure 29. Hardness profile of R17 condition.

3.2.6 Multitrack deposition

As the last objective, the multitrack deposition was performed using the parameters based on R17. For this purpose, five tracks were deposited side by side with an overlap of 74%, a common procedure adopted in DED AM processes [83], followed by the stacking of nine layers on top each other. In total, 50 beads were deposited in a 120 mm long sample exhibited in Figure 30.

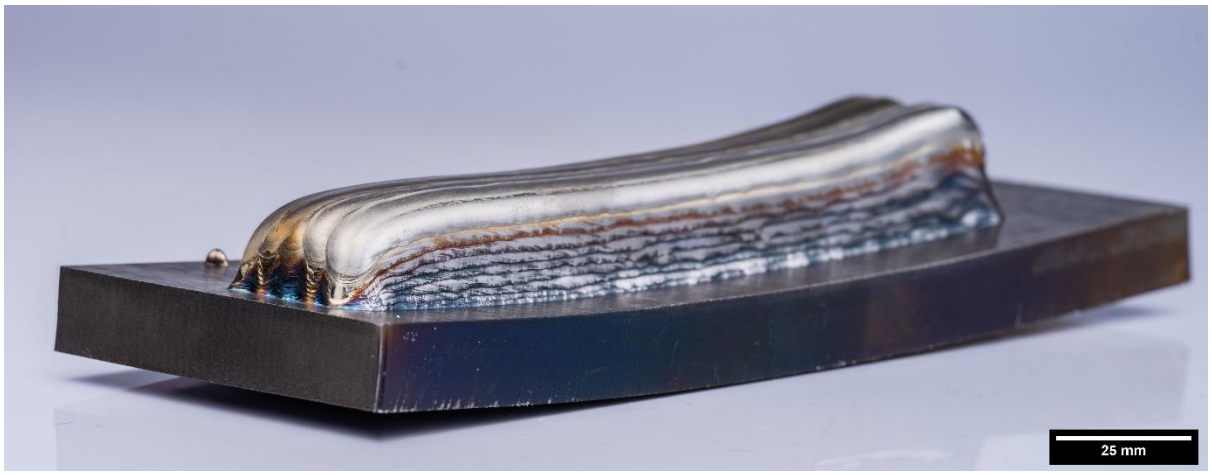

Figure 30. Five-track ten-layer multitrack deposition

The colorful side results from the oxidation, which varies according to the temperature of welding; as the temperature increases the color becomes darker [84]. The warpage of the substrate plate is a collateral effect of high-energy deposition, where thermal stresses lead to high distortions. Nonetheless, it is possible to check a flat and regular

surface, along with a stable build-up without the presence of remarkable/detrimental defects, which might arise as additional difficulties for bulky depositions. This suggests a correct selection of process parameters. Further investigation on the mechanical properties of NiTi processed by EBF3 are envisaged and will be covered in a future work.

4. Conclusions

The investigation of the effect of the process parameters on the manufacturing and properties of Ni-rich NiTi shape memory alloy fabricate by electron beam freeform fabrication was carried out in the present work. For this purpose, a design of experiments by means of the Box-Behnken design was employed, and 17 single-track with one, five, and ten layers were deposited taking into account a range of parameters on beam current, welding speed, and feeding speed. As responses, height, width, dilution and martensitic starting temperature were considered.

The evaluation of build-up parameters' model equation for height and width predicted accurately the validation values, and therefore shown itself reliable. Based on effect of significant factor it was possible to show that i) height is mostly influenced by feeding speed followed by beam current whereas ii) for width mainly beam current followed by welding speed are responsible for most of the remarkable changes. Based on the same equations, the interaction between beam current, welding speed and feeding speed were plotted as contour plots. It was demonstrated that the noticeable variations of height and width resulted from interactions between feeding speed and beam current in both cases.

In the case of dilution and martensitic starting temperature, it was shown that both have a strong linear correlation with energy per volume, increasing in the same fashion with this variable. Since a similarity of curve slopes for both cases was observed, dilution was selected to evaluate the influence of processing on this response. The model equation of dilution presented a high R^2 and adjusted-R^2, showing reliability to predict new values for different process parameters. It was verified by the actual vs. predicted plot, where all points lied within the confidence interval. Feeding speed and beam current were the most influential parameters of the equation, with no influence of welding speed. This fact was observed on the mean effect plot and on the contour plots, and explained based on energy density and material flow. Which by increasing the energy density, there is excessive heat input available, that lead to increase the diameter of melt pool, as a result of that, the ratio of molten base material increase to the molten metal wire, which increases the dilution as well as Martensitic start temperature due to change in chemical composition and evaporation of Ni at high heat input.

The best combination of process parameters was selected based on several criteria considering the flux of energy and material flow, and its impact on surface regularity,

homogeneity of deposition, low dilution and martensitic temperature. Based on it, five conditions were taking into account in a first moment: R3, R7, R12, R15 and R17. Considering the build-up regularity, R12 was eliminated due to its irregular build-up. Further, the humping effect eliminated R3 and R7 since both presented a pronounced effect, and thus compromising the homogeneity of deposition.

The last step of the screening was based on the comparison between R15 and R17. Since R17 presented lower dilution (despite a slightly high martensitic starting temperature) and higher deposition rate - therefore higher productivity keeping satisfactorily the quality –, this condition was selected as the best one. Thus, the following process parameters were selected: 22.5 mA of beam current, 12 mm/sec of welding speed and 3.3 m/min of feeding speed.

The characterization by differential scanning calorimetry of ten-layer deposition based on R17 condition revealed a reversible martensitic to austenitic phase transformation, and therefore the functional properties were present. According to the temperature transitions, austenite was present at room temperature, hence the R17 condition produces superelastic samples. X-ray diffraction made possible to identify austenite (major) and Ti_2Ni (minor) as constituents of the matrix, corroborating the findings of differential scanning calorimetry. The hardness test highlighted the differences between the martensitic base plate and the austenitic deposition, showing a transition zone with lower hardness. The hardness values of the deposition ranged from 260 to 136 HV0.5, values typically found in the literature for additive manufacturing of NiTi.

The last step constituted the multitrack deposition, where a five side-by-side tracks with ten layers each (50 beads in total) specimen was successfully fabricated, showing itself flat, regular and stable. Therefore, one can conclude that the purpose of this work was achieved successfully.

5. Suggestions for future work

The focus of next steps should be on the ageing behavior and mechanical characterization of the EBF3 parts produced using the ideal processing condition. By keeping this objective in mind, multi-track depositions would be necessary to allow extraction of mechanical testing samples. Therefore, the following tests are recommended:

- Thermal treatment: annealing and chemical homogenization followed by ageing treatment at different times to improve the superelastic effect
- Mechanical assessment: the heat treated samples should be tested by compression test to evaluate how the precipitation behavior interfere on the superelastic effect and strain recover

6. Bibliography

[1] F. Froes and R. Boyer, *Additive manufacturing for the aerospace industry*. .

[2] W. E. Frazier, “Metal additive manufacturing: A review,” *J. Mater. Eng. Perform.*, vol. 23, no. 6, pp. 1917–1928, 2014, doi: 10.1007/s11665-014-0958-z.

[3] J. J. Lewandowski and M. Seifi, “Metal Additive Manufacturing: A Review of Mechanical Properties,” *Annu. Rev. Mater. Res.*, vol. 46, no. 1, pp. 151–186, 2016, doi: 10.1146/annurev-matsci-070115-032024.

[4] T. DebRoy *et al.*, “Additive manufacturing of metallic components – Process, structure and properties,” *Prog. Mater. Sci.*, vol. 92, pp. 112–224, 2018, doi: 10.1016/j.pmatsci.2017.10.001.

[5] M. H. Elahinia, M. Hashemi, M. Tabesh, and S. B. Bhaduri, “Manufacturing and processing of NiTi implants: A review,” *Prog. Mater. Sci.*, vol. 57, no. 5, pp. 911–946, Jun. 2012, doi: 10.1016/j.pmatsci.2011.11.001.

[6] R. Bogue, “Shape-memory materials: A review of technology and applications,” *Assem. Autom.*, vol. 29, no. 3, pp. 214–219, 2009, doi: 10.1108/01445150910972895.

[7] M. Elahinia, N. Shayesteh Moghaddam, M. Taheri Andani, A. Amerinatanzi, B. A. Bimber, and R. F. Hamilton, “Fabrication of NiTi through additive manufacturing: A review,” *Prog. Mater. Sci.*, vol. 83, pp. 630–663, Oct. 2016, doi: 10.1016/j.pmatsci.2016.08.001.

[8] C. Haberland, H. Meier, and J. Frenzel, “On the properties of Ni-rich NiTi shape memory parts produced by selective laser melting,” in *ASME 2012 Conference on Smart Materials, Adaptive Structures and Intelligent Systems, SMASIS 2012*, Sep. 2012, vol. 1, pp. 97–104, doi: 10.1115/SMASIS2012-8040.

[9] C. Haberland, M. Elahinia, J. M. Walker, H. Meier, and J. Frenzel, “On the development of high quality NiTi shape memory and pseudoelastic parts by additive manufacturing,” *Smart Mater. Struct.*, vol. 23, no. 10, p. 104002, Oct. 2014, doi: 10.1088/0964-1726/23/10/104002.

[10] M. Elahinia *et al.*, “Additive manufacturing of NiTiHf high temperature shape memory alloy,” *Scr. Mater.*, vol. 145, pp. 90–94, 2018, doi: 10.1016/j.scriptamat.2017.10.016.

[11] S. Dadbakhsh, M. Speirs, J. P. Kruth, J. Schrooten, J. Luyten, and J. Van Humbeeck, “Effect of SLM parameters on transformation temperatures of shape memory nickel titanium parts,” *Adv. Eng. Mater.*, vol. 16, no. 9, pp. 1140–1146,

Sep. 2014, doi: 10.1002/adem.201300558.

[12] S. Dadbakhsh, B. Vrancken, J. P. Kruth, J. Luyten, and J. Van Humbeeck, “Texture and anisotropy in selective laser melting of NiTi alloy,” *Mater. Sci. Eng. A*, vol. 650, pp. 225–232, 2016, doi: 10.1016/j.msea.2015.10.032.

[13] J. Fuchs, C. Schneider, and N. Enzinger, “Wire-based additive manufacturing using an electron beam as heat source,” *Weld. World*, vol. 62, no. 2, pp. 267–275, 2018, doi: 10.1007/s40194-017-0537-7.

[14] D. Ding, Z. Pan, D. Cuiuri, and H. Li, “Wire-feed additive manufacturing of metal components: technologies, developments and future interests,” *Int. J. Adv. Manuf. Technol.*, vol. 81, no. 1–4, pp. 465–481, 2015, doi: 10.1007/s00170-015-7077-3.

[15] R. K. Bird and J. Hibberd, “Tensile Properties and Microstructure of Inconel 718 Fabricated with Electron Beam Freeform Fabrication (EBF3),” no. September 2009, pp. 1–19, 2009, doi: NASA/TM-2009-215929.

[16] J. Xu, J. Zhu, J. Fan, Q. Zhou, Y. Peng, and S. Guo, “Microstructure and mechanical properties of Ti–6Al–4V alloy fabricated using electron beam freeform fabrication,” *Vacuum*, vol. 167, pp. 364–373, Sep. 2019, doi: 10.1016/j.vacuum.2019.06.030.

[17] J. Fuchs, C. Schneider, and N. Enzinger, “Wire-based additive manufacturing using an electron beam as heat source,” *Weld. World*, vol. 62, no. 2, pp. 267–275, 2018, doi: 10.1007/s40194-017-0537-7.

[18] M. S. Domack, K. M. Taminger, and M. Begley, “Metallurgical Mechanisms Controlling Mechanical Properties of Aluminium Alloy 2219 Produced by Electron Beam Freeform Fabrication,” *Mater. Sci. Forum*, vol. 519–521, no. September 2006, pp. 1291–1296, 2006, doi: 10.4028/www.scientific.net/msf.519-521.1291.

[19] K. M. B. Taminger, R. A. Hafley, and M. S. Domack, “Evolution and Control of 2219 Aluminium Microstructural Features through Electron Beam Freeform Fabrication,” *Mater. Sci. Forum*, vol. 519–521, no. March 2006, pp. 1297–1302, 2006, doi: 10.4028/www.scientific.net/MSF.519-521.1297.

[20] M. T. Stawovy, “Comparison of LCAC and PM Mo deposited using Sciaky EBAM™,” *Int. J. Refract. Met. Hard Mater.*, vol. 73, no. February, pp. 162–167, Jun. 2018, doi: 10.1016/j.ijrmhm.2018.02.009.

[21] Q. Tang, S. Pang, B. Chen, H. Suo, and J. Zhou, “A three dimensional transient

model for heat transfer and fluid flow of weld pool during electron beam freeform fabrication of Ti-6-Al-4-V alloy," *Int. J. Heat Mass Transf.*, vol. 78, pp. 203–215, Nov. 2014, doi: 10.1016/j.ijheatmasstransfer.2014.06.048.

[22] J. L. Beuth *et al.*, "Process Mapping for Qualification Across Multiple Direct Metal Additive Manufacturing Processes," *Proc. Solid Free. Fabr. Symp.*, pp. 655–665, 2014, doi: 10.1007/s13398-014-0173-7.2.

[23] X. Shu, G. Chen, J. Liu, B. Zhang, and J. Feng, "Microstructure evolution of copper/steel gradient deposition prepared using electron beam freeform fabrication," *Mater. Lett.*, vol. 213, pp. 374–377, Feb. 2018, doi: 10.1016/j.matlet.2017.11.016.

[24] J. Dutkiewicz, Ł. Rogal, D. Kalita, and M. We, "Superelastic Effect in NiTi Alloys Manufactured Using Electron Beam and Focused Laser Rapid Manufacturing Methods," no. Ref 10, 2020, doi: 10.1007/s11665-020-04938-z.

[25] J. Mohd Jani, M. Leary, A. Subic, and M. A. Gibson, "A review of shape memory alloy research, applications and opportunities," *Mater. Des.*, vol. 56, pp. 1078–1113, Apr. 2014, doi: 10.1016/J.MATDES.2013.11.084.

[26] R. Dasgupta, "A look into Cu-based shape memory alloys: Present scenario and future prospects," *J. Mater. Res.*, vol. 29, no. 16, pp. 1681–1698, 2014, doi: 10.1557/jmr.2014.189.

[27] C. Haberland, M. Elahinia, J. M. Walker, H. Meier, and J. Frenzel, "On the development of high quality NiTi shape memory and pseudoelastic parts by additive manufacturing," *Smart Mater. Struct.*, vol. 23, no. 10, 2014, doi: 10.1088/0964-1726/23/10/104002.

[28] K. Yamauchi, I. Ohkata, K. Tsuchiya, and S. Miyazaki, *Shape memory and superelastic alloys: Technologies and applications*. 2011.

[29] S. Dadbakhsh, M. Speirs, J. Van Humbeeck, and J. P. Kruth, "Laser additive manufacturing of bulk and porous shape-memory NiTi alloys: From processes to potential biomedical applications," *MRS Bull.*, vol. 41, no. 10, pp. 765–774, Oct. 2016, doi: 10.1557/mrs.2016.209.

[30] K. Dai and C. Ning, "Shape memory alloys and their medical applications," in *Biomechanics and Biomaterials in Orthopedics, Second Edition*, 2016, pp. 187–195.

[31] D. J. Hartl and D. C. Lagoudas, "Aerospace applications of shape memory alloys," *Proc. Inst. Mech. Eng. Part G J. Aerosp. Eng.*, vol. 221, no. 4, pp. 535–

552, Apr. 2007, doi: 10.1243/09544100JAERO211.

[32] K. Otsuka and X. Ren, “Physical metallurgy of Ti–Ni-based shape memory alloys,” *Prog. Mater. Sci.*, vol. 50, no. 5, pp. 511–678, Jul. 2005, doi: 10.1016/j.pmatsci.2004.10.001.

[33] P. S. Lobo, J. Almeida, and L. Guerreiro, “Shape Memory Alloys Behaviour: A Review,” *Procedia Eng.*, vol. 114, pp. 776–783, 2015, doi: 10.1016/j.proeng.2015.08.025.

[34] J. Frenzel, E. P. George, A. Dlouhy, C. Somsen, M. F. X. Wagner, and G. Eggeler, “Influence of Ni on martensitic phase transformations in NiTi shape memory alloys,” *Acta Mater.*, vol. 58, no. 9, pp. 3444–3458, May 2010, doi: 10.1016/j.actamat.2010.02.019.

[35] J. W. Mwangi, L. T. Nguyen, V. D. Bui, T. Berger, H. Zeidler, and A. Schubert, “Nitinol manufacturing and micromachining: A review of processes and their suitability in processing medical-grade nitinol,” *J. Manuf. Process.*, vol. 38, pp. 355–369, Feb. 2019, doi: 10.1016/J.JMAPRO.2019.01.003.

[36] R. H. F. Lima, J. S., Neto, A. C. W. & Melo, “Friction Stir Welding of Austenitic NiTi Shape,” *Glob. J. Res. Eng. J - Gen. Eng.*, vol. 17, no. 1, 2017, [Online]. Available: https://globaljournals.org/GJRE_Volume17/1-Friction-Stir-Welding-of-Austenitic.pdf.

[37] J. P. Oliveira, J. F. Duarte, P. Inácio, N. Schell, R. M. Miranda, and T. G. Santos, “Production of Al/NiTi composites by friction stir welding assisted by electrical current,” *Mater. Des.*, vol. 113, pp. 311–318, Jan. 2017, doi: 10.1016/j.matdes.2016.10.038.

[38] D. Herzog, V. Seyda, E. Wycisk, and C. Emmelmann, “Additive manufacturing of metals,” *Acta Mater.*, vol. 117, pp. 371–392, Sep. 2016, doi: 10.1016/j.actamat.2016.07.019.

[39] Y. Kok *et al.*, “Anisotropy and heterogeneity of microstructure and mechanical properties in metal additive manufacturing: A critical review,” *Mater. Des.*, vol. 139, pp. 565–586, 2018, doi: 10.1016/j.matdes.2017.11.021.

[40] P. K. Gokuldoss, S. Kolla, and J. Eckert, “Additive manufacturing processes: Selective laser melting, electron beam melting and binder jetting-selection guidelines,” *Materials (Basel).*, vol. 10, no. 6, 2017, doi: 10.3390/ma10060672.

[41] W. J. Sames, F. A. List, S. Pannala, R. R. Dehoff, and S. S. Babu, “The metallurgy and processing science of metal additive manufacturing,” *Int. Mater.*

Rev., vol. 61, no. 5, pp. 315–360, 2016, doi: 10.1080/09506608.2015.1116649.

[42] M. Bram, M. Bitzer, H. P. Buchkremer, and D. Stöver, “Reproducibility study of niti parts made by metal injection molding,” *J. Mater. Eng. Perform.*, vol. 21, no. 12, pp. 2701–2712, 2012, doi: 10.1007/s11665-012-0264-6.

[43] M. H. Ismail, R. Goodall, H. A. Davies, and I. Todd, “Porous NiTi alloy by metal injection moulding/sintering of elemental powders: Effect of sintering temperature,” *Mater. Lett.*, vol. 70, pp. 142–145, 2012, doi: 10.1016/j.matlet.2011.12.008.

[44] L. C. Zhang, Y. Liu, S. Li, and Y. Hao, “Additive Manufacturing of Titanium Alloys by Electron Beam Melting: A Review,” *Adv. Eng. Mater.*, vol. 20, no. 5, pp. 1–16, 2018, doi: 10.1002/adem.201700842.

[45] Z. X. Khoo, Y. Liu, J. An, C. K. Chua, Y. F. Shen, and C. N. Kuo, “A review of selective laser melted NiTi shape memory alloy,” *Materials (Basel).*, vol. 11, no. 4, pp. 11–17, Mar. 2018, doi: 10.3390/ma11040519.

[46] A. T. Clare, P. R. Chalker, S. Davies, C. J. Sutcliffe, and S. Tsopanos, “Selective laser melting of high aspect ratio 3D nickel-titanium structures two way trained for MEMS applications,” *Int. J. Mech. Mater. Des.*, vol. 4, no. 2, pp. 181–187, Jun. 2008, doi: 10.1007/s10999-007-9032-4.

[47] M. H. Elahinia, *Shape Memory Alloy Actuators: Design, Fabrication and Experimental Evaluation*. Chichester, UK: John Wiley & Sons, Ltd, 2015.

[48] S. Dudziak, M. Gieseke, H. Haferkamp, S. Barcikowski, and D. Kracht, “Functionality of laser-sintered shape memory micro-actuators,” *Phys. Procedia*, vol. 5, no. PART 2, pp. 607–615, 2010, doi: 10.1016/j.phpro.2010.08.088.

[49] Z. Zeng *et al.*, “Wire and arc additive manufacturing of a Ni-rich NiTi shape memory alloy: Microstructure and mechanical properties,” *Addit. Manuf.*, vol. 32, no. January, 2020, doi: 10.1016/j.addma.2020.101051.

[50] J. K. Watson, K. M. B. Taminger, R. A. Hafley, and D. D. Petersen, “Development of a prototype low-voltage electron beam freeform fabrication,” in *Solid Freeform Fabrication Proceedings (2002) 458-465*, 2002, no. 2002, p. 21, Accessed: Jun. 29, 2020. [Online]. Available: https://www.researchgate.net/publication/239220871_DEVELOPMENT_OF_A_PROTOTYPE_LOW-VOLTAGE_ELECTRON_BEAM_FREEFORM_FABRICATION_SYSTEM.

[51] R. A. Hafley, K. M. B. Taminger, and R. K. Bird, “Electron beam freeform

fabrication in the space environment," in *45th AIAA Aerospace Meeting and Exhibit*, 2007, no. January, pp. 1–9.

[52] T. A. Wallace, K. S. Bey, and K. M. B. Taminger, "A Design of Experiments Approach Defining the Relationships Between Processing and Microstructure for Ti-6Al-4V," *Proc. 15th Symp. Solid Free. Fabr.*, pp. 104–115, 2004.

[53] Sciaky Inc., "Wirefeed Additive Manufacturing vs. Powder Methods | Sciaky," 2018. http://www.sciaky.com/additive-manufacturing/wire-am-vs-powder-am (accessed Dec. 12, 2018).

[54] P. D. B. Baufeld, R. Widdison, and T. Dutilleul, "Wire based electron beam additive manufacturing," *Baufeld, Bernd Widdison, R Dutilleul, T*, pp. 1–8, 2017.

[55] K. M. Taminger and R. A. Hafley, "Electron Beam Freeform Fabrication for Cost Effective Near-Net Shape Manufacturing," *Spec. Meet. Cost Eff. Manuf. via Net Shape Process. (NATO/RTO AVT-139)*, pp. 16:1–10, 2006, doi: 10.1016/j.clinph.2008.07.218.

[56] K. Taminger and R. Hafley, "Electron beam freeform fabrication: a rapid metal deposition process," *Proc. 3rd Annu. Automot. Compos. Conf.*, no. 2003, pp. 9–10, 2003, [Online]. Available: http://www.ntrs.nasa.gov/archive/nasa/casi.ntrs.nasa.gov/20040042496_2004036110.pdf.

[57] K. M. B. Taminger, R. A. Hafley, D. T. Fahringer, and R. E. Martin, "Effect of Surface Treatments on Electron Beam Freeform Fabricated Aluminum Structures," vol. 2219, 2004.

[58] D. Ding, Z. Pan, D. Cuiuri, and H. Li, "Wire-feed additive manufacturing of metal components: technologies, developments and future interests," *Int. J. Adv. Manuf. Technol.*, vol. 81, no. 1–4, pp. 465–481, Oct. 2015, doi: 10.1007/s00170-015-7077-3.

[59] K. M. B. Taminger and R. A. Hafley, "Characterization od 2219 aluminum produced by electron beam freeform fabrication," in *13th Solid Freeform Fabrication Symposiom*, 2002, pp. 14–15, [Online]. Available: https://ntrs.nasa.gov/archive/nasa/casi.ntrs.nasa.gov/20030012702.pdf.

[60] P. Zelinski, "The Possibilities of Electron Beam Additive Manufacturing : Additive Manufacturing Magazine," *Additive Manufacturing*, 2016. https://www.additivemanufacturing.media/articles/the-possibilities-of-electron-beam-additive-manufacturing (accessed Dec. 12, 2018).

[61] S. T. Amancio-Filho and L. A. Blaga, *Joining of polymer-metal hybrid structures: Principles and applications*. Hoboken, NJ: John Wiley & Sons, Inc, 2018.

[62] M. C. D. & A.-C. C. C. Myers H Raymond, *Response Surface Methodology: Process and Product Optimization Using ...* -. John Wiley & Sons, 2016, 2016.

[63] J. Zolgharnein, A. Shahmoradi, and J. B. Ghasemi, “Comparative study of Box-Behnken, central composite, and Doehlert matrix for multivariate optimization of Pb (II) adsorption onto Robinia tree leaves,” *J. Chemom.*, vol. 27, no. 1–2, pp. 12–20, 2013, doi: 10.1002/cem.2487.

[64] E. E. Feistauer, J. F. dos Santos, and S. T. Amancio-Filho, “An investigation of the ultrasonic joining process parameters effect on the mechanical properties of metal-composite hybrid joints,” *Weld. World*, 2020, doi: 10.1007/s40194-020-00927-x.

[65] S. L. C. Ferreira *et al.*, “Box-Behnken design: An alternative for the optimization of analytical methods,” *Anal. Chim. Acta*, vol. 597, no. 2, pp. 179–186, 2007, doi: 10.1016/j.aca.2007.07.011.

[66] R. D. S. G. Campilho, L. F. M. da Silva, and M. D. Banea, *Adhesive bonding of polymer composites to lightweight metals*. 2018.

[67] P. R. Peter, “Drahtbasiertes additives Fertigen von Ti6AlV4 mittels Elektronenstrahlschweißen,” Graz University of Technology, 2017.

[68] J. Fuchs, “Drahtbasierte additive Fertigung mit dem Elektronenstrahl und einer unlegierten Massivdrahtelektrode,” Graz University of Technology, 2016.

[69] M. D. Abràmoff, P. J. Magalhães, and S. J. Ram, “Image processing with imageJ,” *Biophotonics Int.*, vol. 11, no. 7, pp. 36–41, 2004, doi: 10.1201/9781420005615.ax4.

[70] Association For Testing Materials - ASTM, “ASTM F2004 - 05(2010) Standard Test Method for Transformation Temperature of Nickel-Titanium Alloys by Thermal Analysis,” 2010. https://www.astm.org/Standards/F2004.htm (accessed Apr. 15, 2019).

[71] L. Lutterotti, R. Vasin, and H. R. Wenk, “Rietveld texture analysis from synchrotron diffraction images. I. Calibration and basic analysis,” *Powder Diffr.*, vol. 29, no. 1, pp. 76–84, Mar. 2014, doi: 10.1017/S0885715613001346.

[72] A. J. Pinkerton, “Laser direct metal deposition: Theory and applications in manufacturing and maintenance,” *Adv. Laser Mater. Process. Technol. Res. Appl.*, pp. 461–491, 2010, doi: 10.1533/9781845699819.6.461.

[73] P. Berger, H. Hügel, A. Hess, R. Weber, and T. Graf, “Understanding of humping based on conservation of volume flow,” *Phys. Procedia*, vol. 12, no. PART 1, pp. 232–240, 2011, doi: 10.1016/j.phpro.2011.03.030.

[74] Adebayo A, J. Mehnen, and X. Tonnellier, “Limiting travel speed in additive layer manufacturing,” *ASM Proc. Int. Conf. Trends Weld. Res.*, vol. 3, pp. 1038–1044, 2013.

[75] J. M. Walker, C. Haberland, M. Taheri Andani, H. E. Karaca, D. Dean, and M. Elahinia, “Process development and characterization of additively manufactured nickel-titanium shape memory parts,” *J. Intell. Mater. Syst. Struct.*, vol. 27, no. 19, pp. 2653–2660, 2016, doi: 10.1177/1045389X16635848.

[76] N. S. Moghaddam *et al.*, “Achieving superelasticity in additively manufactured NiTi in compression without post-process heat treatment,” *Sci. Reports - Revis.*, vol. 9, no. 1, p. 41, Dec. 2018, doi: 10.1038/s41598-018-36641-4.

[77] X. Wang, X. Gong, and K. Chou, “Scanning Speed Effect on Mechanical Properties of Ti-6Al-4V Alloy Processed by Electron Beam Additive Manufacturing,” in *Procedia Manufacturing*, Jan. 2015, vol. 1, pp. 287–295, doi: 10.1016/j.promfg.2015.09.026.

[78] S. Dahat, K. Hurtig, J. Andersson, and A. Scotti, “A methodology to parameterize wire + arc additive manufacturing: A case study for wall quality analysis,” *J. Manuf. Mater. Process.*, vol. 4, no. 1, 2020, doi: 10.3390/jmmp4010014.

[79] J. Walker, M. Elahinia, and C. Haberland, “An Investigation of Process Parameters on Selective Laser Melting of Nitinol,” p. V001T01A007, 2014, doi: 10.1115/smasis2013-3074.

[80] B. Lu *et al.*, “Direct rapid prototyping of shape memory alloy with linear superelasticity via plasma arc deposition,” *Vacuum*, vol. 157, pp. 65–68, Nov. 2018, doi: 10.1016/j.vacuum.2018.08.028.

[81] L. Lecce and A. Concilio, Eds., *Shape Memory Alloy Engineering: For Aerospace, Structural and Biomedical Applications*. Butterworth-Heinemann, 2015.

[82] J. Wang, Z. Pan, G. Yang, J. Han, X. Chen, and H. Li, “Location dependence of microstructure, phase transformation temperature and mechanical properties on Ni-rich NiTi alloy fabricated by wire arc additive manufacturing,” *Mater. Sci. Eng. A*, vol. 749, no. December 2018, pp. 218–222, 2019, doi: 10.1016/j.msea.2019.02.029.

[83] S. van Duin, D. Cuiuri, H. Li, D. Ding, Z. Pan, and N. Larkin, “Bead modelling and implementation of adaptive MAT path in wire and arc additive manufacturing,” *Robot. Comput. Integr. Manuf.*, vol. 39, pp. 32–42, 2015, doi: 10.1016/j.rcim.2015.12.004.

[84] B. C. de ALMEIDA and C. N. ELIAS, “Influence of heat treatment on color and flexibility of nickel-titanium endodontic instruments,” *RGO - Rev. Gaúcha Odontol.*, vol. 68, 2020, doi: 10.1590/1981-86372020000443683.

7. Appendix

Equation for the martensitic starting temperature, Ms:

$$\begin{aligned} \mathrm{Ms} = -212 + 33.8 * \mathrm{BC} - \ 19.6 * \mathrm{WS} - \ 80 * \mathrm{FS} - 0.046 * \mathrm{BC}^2 0.26 * \\ \mathrm{WS}^2 + 33.3 * \mathrm{FS}^2 + 0.385 * \mathrm{BC} * \mathrm{WS} - 9.62 * \mathrm{BC} * \mathrm{FS} + 5.89 * \mathrm{WS} * \mathrm{FS} \end{aligned} \quad (12)$$

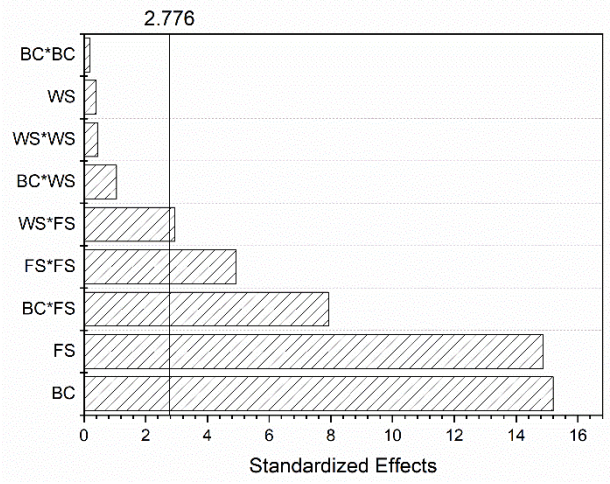

Figure 31. Pareto chart for the standardized effects of the model for Ms.

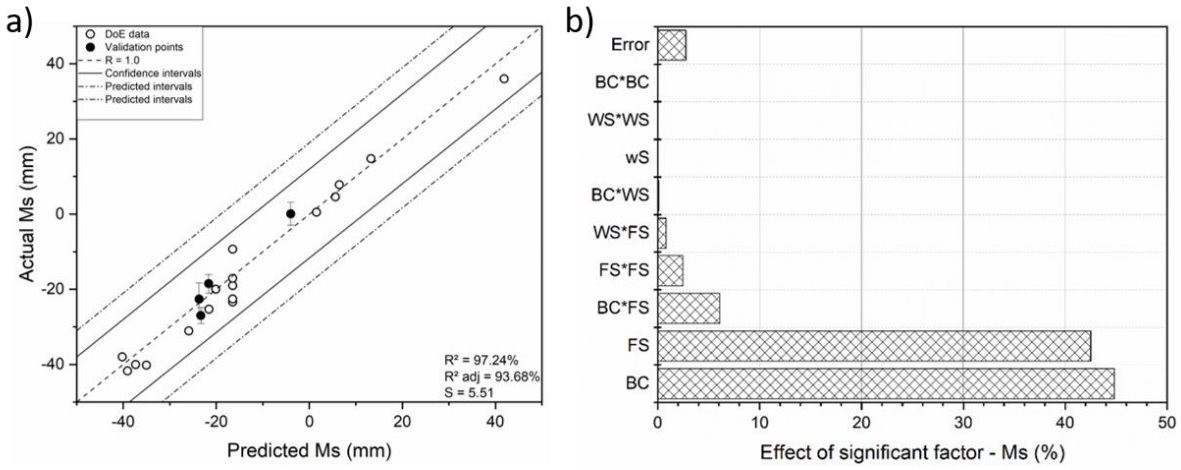

Figure 32. a) Actual versus predicted diagram for the Ms model and b) effect of each significant factor on the model.

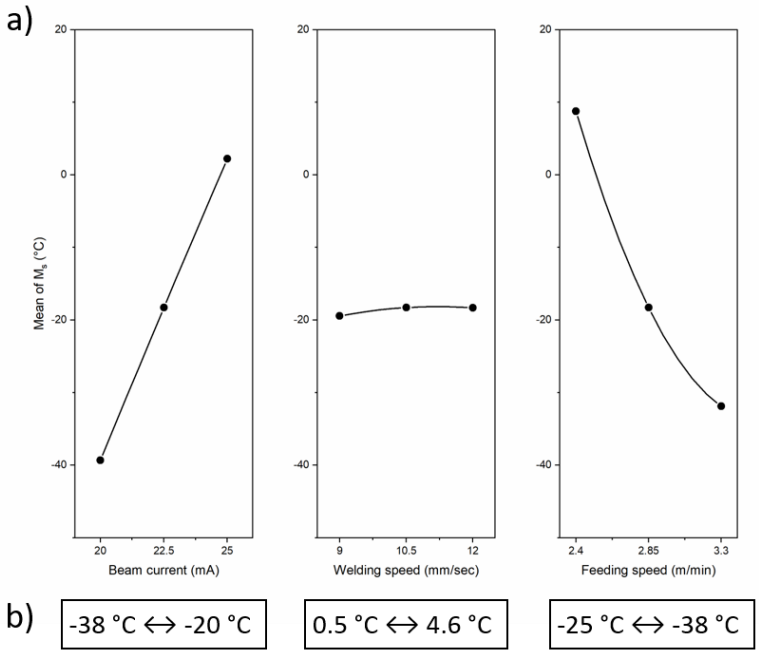

Figure 33. a) Mean effect plot of the process parameters on Ms and b) related temperatures of high and low limits of each individual parameter evaluated within the BBD. For beam current, the minimum and maximum correspond to R12 and R8, respectively. For welding speed, the minimum and maximum correspond to R5 and R5, respectively. For feeding speed, the minimum and maximum correspond to R10 and R12, respectively.

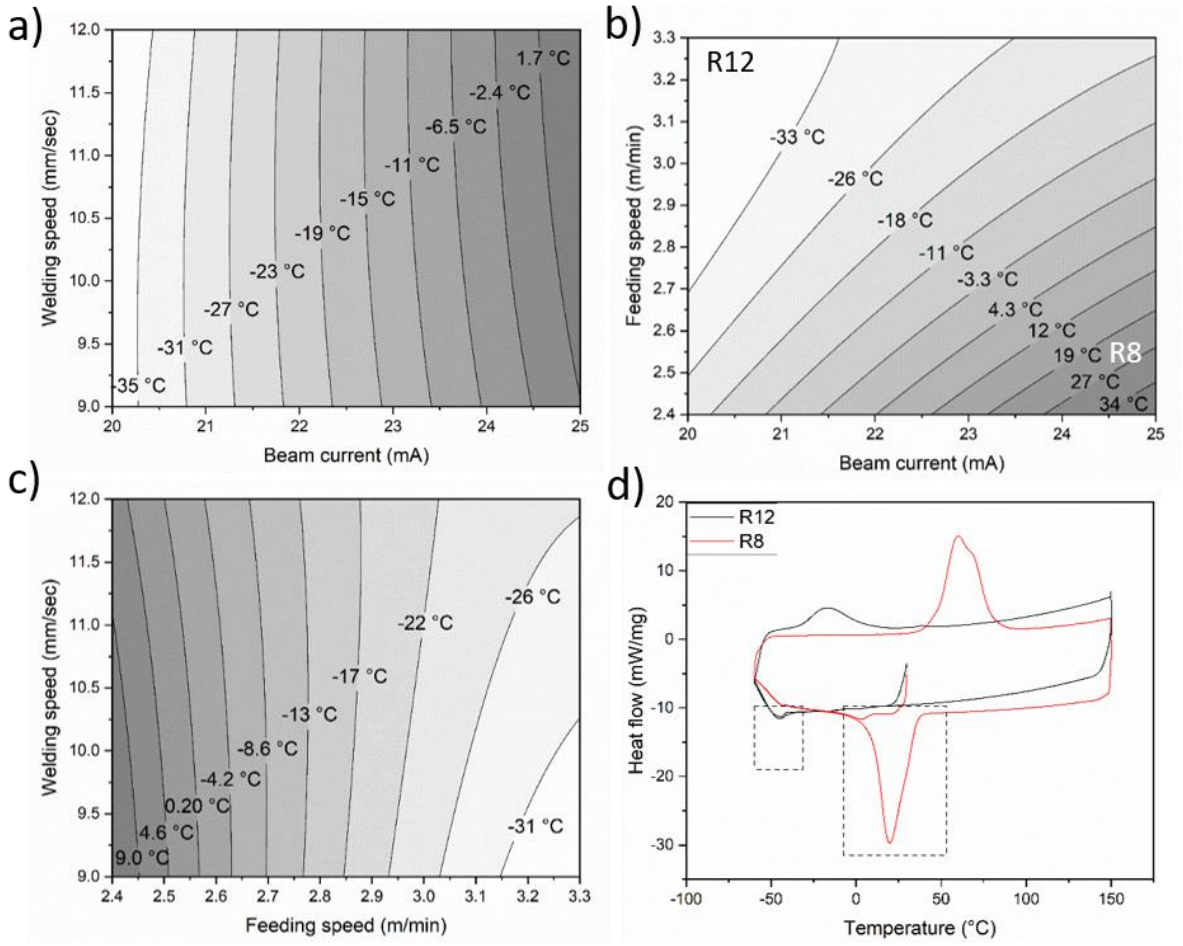

Figure 34. Contour plot of two-way interactions where each contour line is related to Ms (°C). In (a) welding speed versus beam current, (b) feeding speed versus beam current, and (c) welding speed versus feeding speed. R12 and R8 in (b) are the DSC complete cycle.